

**UNIFIED INSTRUMENTATION: EXAMINING THE SIMULTANEOUS  
APPLICATION OF ADVANCED MEASUREMENT TECHNIQUES  
FOR INCREASED WIND TUNNEL TESTING CAPABILITY**

Gary A. Fleming, Editor

**Unified Instrumentation Team Members:**

Scott M. Bartram, Gary A. Fleming, William M. Humphreys, Jr., Luther N. Jenkins, Jeffrey D. Jordan,  
Joseph W. Lee, Bradley D. Leighty, James F. Meyers, and Bruce W. South

*National Aeronautics and Space Administration  
Langley Research Center  
Hampton, Virginia, 23681-2199 USA*

Angelo A. Cavone, JoAnne L. Ingram, Mark A. Kulick, Donald M. Oglesby,  
Richard J. Schwartz, A. Neal Watkins

*Swales Aerospace, Inc.  
Langley Research Center  
Hampton, Virginia, 23681-2199 USA*

**ABSTRACT**

A Unified Instrumentation Test examining the combined application of Pressure Sensitive Paint, Projection Moiré Interferometry, Digital Particle Image Velocimetry, Doppler Global Velocimetry, and Acoustic Microphone Array has been conducted at the NASA Langley Research Center. The fundamental purposes of conducting the test were to (a) identify and solve compatibility issues among the techniques that would inhibit their simultaneous application in a wind tunnel, and (b) demonstrate that simultaneous use of advanced instrumentation techniques is feasible for increasing tunnel efficiency and identifying control surface actuation / aerodynamic reaction phenomena. This paper provides summary descriptions of each measurement technique used during the Unified Instrumentation Test, their implementation for testing in a unified fashion, and example results identifying areas of instrument compatibility and incompatibility. Conclusions are drawn regarding the conditions under which the measurement techniques can be operated simultaneously on a non-interference basis. Finally,

areas requiring improvement for successfully applying unified instrumentation in future wind tunnel tests are addressed.

**INTRODUCTION**

The NASA Aeronautics Blueprint<sup>1</sup> identifies the development of *revolutionary vehicles with significantly greater performance* as a critical element required to alleviate an already burdened U.S. airspace system and maintain U.S. aviation leadership. Conceptually, these revolutionary vehicles will be comprised of a morphing airframe and various active flow, noise, and flight control systems that adapt themselves for optimal performance in each flight regime. Ground testing and validation of such a complicated vehicle will require far more than conventional aerodynamic force and moment data collected during wind tunnel tests. Highly advanced wind tunnel instrumentation systems will be required, and their development must precede the technology that they are intended to validate.

The next generation of wind tunnel instrumentation systems will be required to obtain simultaneous global measurements of multiple unsteady physical phenomena. This criterion is predicated by two fundamental needs: (1) the need to measure and understand the relationship between control system

---

Copyright © 2002 by the American Institute of Aeronautics and Astronautics, Inc. No copyright is asserted in the United States under Title 17, U.S. Code. The U.S. Government has a royalty-free license to exercise all rights under the copyright claimed herein for Governmental purposes. All other rights are reserved by the copyright owner.

actuation and aerodynamic reaction, and (2) the continual need to increase wind tunnel testing efficiency by maximizing the knowledge gathered during the course of the test. Examining the combined use of existing instrumentation systems is a first step in satisfying both of these needs.

A large number of diagnostic methods currently exist for measuring specific physical properties during wind tunnel testing. A majority of these techniques, particularly those that are optical in nature, have been developed without considering compatibility issues with other instrumentation systems. Such techniques have historically been applied serially during wind tunnel tests, drastically increasing tunnel testing time and cost by requiring duplicate runs for each instrument. Testing in this manner also reduced or eliminated the possibility of examining aerodynamic cause/effect relationships that could have been detected if multiple instruments were applied simultaneously. However, with careful engineering, some of these techniques can be configured to be compatible with each other, allowing for simultaneous use during wind tunnel tests. In addition to reducing tunnel run time, this restores the possibility of observing aerodynamic phenomena that might not be revealed when using a single measurement method.

A research effort chartered to investigate compatibility issues among various advanced wind tunnel instrumentation techniques has been conducted at the NASA Langley Research Center (LaRC) since 1998. This effort, named the Unified Instrumentation Project, has had the goal of removing instrument incompatibilities to facilitate the development of a suite of compatible measurement techniques that can be selectively used by aero researchers. The project has recently culminated in a Unified Instrumentation Test where multiple advanced instrumentation techniques were simultaneously applied to measure off-body flow velocity, on-body pressure, and structural deformation of a flat plate with hinged leading edge. The techniques used include Digital Particle Image Velocimetry (DPIV), Doppler Global Velocimetry (DGV), Pressure Sensitive Paint (PSP), Projection Moiré Interferometry (PMI), and a 80-sensor Acoustic Microphone Array (AMA). The fundamental purposes of conducting the test were to (a) identify and solve compatibility issues among the techniques used that would inhibit their simultaneous application in a wind tunnel, and (b) demonstrate that simultaneous use of advanced optical instrumentation techniques is feasible for increasing tunnel efficiency and identifying control surface actuation / aerodynamic reaction phenomena.

Additionally, the test has revealed fundamental insights regarding the physical and practical interactions between each instrumentation system. These insights have been used to identify ways to remove instrument incompatibilities/redundancies for efficient application of unified instrumentation in future wind tunnel tests.

This paper provides summary descriptions of the experimental facilities, model, and instrumentation techniques used in the Unified Instrumentation Test. Sample data gathered by each instrument when operated in a unified testing scenario are presented to illustrate areas of instrument compatibility and incompatibility. Conclusions are provided as to which instrumentation systems can be operated simultaneously on a non-interference basis, and what practical implementation issues need to be addressed to facilitate the use of unified instrumentation in the future.

## **MEASUREMENT TECHNIQUES SUMMARY**

### **Virtual Facilities (VF)**

VF refers to the use of three-dimensional computer modeling to visualize a wind tunnel test environment. Although not considered a true wind tunnel diagnostic technique, VF technology has proven useful in planning the implementation of various optical instrumentation systems in numerous wind tunnel tests. VF models constructed for the Unified Instrumentation Test were used to determine the optimal hardware configurations for each measurement technique involved. This required balancing the instrumentation needs with the spatial and optical constraints imposed by the facility, while ensuring the instrumentation systems could co-exist without interfering with each other. The VF models also provided enhanced post-test data analysis and visualization capabilities by allowing researchers to import processed data back into the virtual environment.

VF models are generated using commercially available computer animation and rendering software. This software enables the user to merge accurate three-dimensional wind tunnel geometries with the CAD files developed to fabricate the wind tunnel model being tested<sup>2</sup>. Once the test configuration has been created in the virtual environment, optimal placement of the instrumentation components can be determined by simulating their positions about the test section. For camera-based instrumentation systems, the ability of the software to simulate photo-realistic camera views allows the researcher to visualize the measurement area

observed by each camera<sup>3</sup>. This aids in determining whether the proper field-of-view can be obtained for a given mounting position, if there are obstructions to the field-of-view, and if adequate illumination will exist. Each candidate instrument configuration is tested as the virtual wind tunnel model is animated through its test matrix, such as an angle-of-attack sweep. This provides the ability to determine if optical access to the region-of-interest can be maintained throughout the test envelope. Designing instrument configurations in this manner can isolate problems that may be encountered during testing and provide the researcher the capability to explore solutions without the expense of additional tunnel occupancy time.

**On-body: Acoustic Microphone Array (AMA)**

Full assessment of complex separated flows above a model often requires the global measurement of the unsteady dynamic pressure on the model surface. This can be accomplished by using a two-dimensional AMA<sup>4</sup>. The microphones constituting the array serve as hydrodynamic pressure sensors whose response is proportional to the *unsteady* component of the surface dynamic pressure. The microphones are typically embedded within the model, flush-mounted with the model surface. Analyzing the time-dependent data simultaneously acquired from all microphones in the array can provide insight into relationships between the on-body pressure distribution and the off-body flow characteristics<sup>5</sup>. For example, flow reattachment location can be deduced by examining the root-mean-square (RMS) pressure fluctuations computed from the microphone outputs<sup>6</sup>. The reattachment location generally corresponds to the location where the RMS pressure fluctuations are at a maximum. The data can be further analyzed in the frequency domain to allow examination of auto-spectra, cross-spectra, and coherence, providing insight into the flow turbulence convective velocities and large eddy sizes<sup>4-5</sup>. Use of the AMA in the Unified Instrumentation Test allowed for the comparison of the measured flow reattachment location using on- and off-body flow diagnostic techniques.

**On-body: Pressure Sensitive Paint (PSP)**

PSP measurement techniques have been employed for the global measurement of time-averaged surface pressure distributions on aerodynamic test articles for over two decades, and are currently used in production mode in several wind tunnel facilities worldwide<sup>7-17</sup>. The wide use and maturity of PSP makes it an ideal

candidate for simultaneous use with other measurement methods. PSP was included during the Unified Instrumentation Test to determine if it could be used simultaneously with PMI and off-body flow diagnostic techniques requiring flow seeding. This would provide the capability to establish relationships between the on-body global surface pressure distribution and off-body flow characteristics.

PSP techniques exploit the oxygen sensitivity of luminescent probe molecules (luminophores) that are dispersed within gas-permeable paints<sup>18</sup>. This process is shown schematically in figure 1. Under appropriate illumination, typically 300 – 500 nm wavelength light, the luminophore molecules absorb photons from the illumination source and emit them at wavelengths from 600 – 750 nm. The intensity of the luminophore emission is inversely proportional to the oxygen concentration, and hence pressure, at the surface. Global pressure measurements can thus be obtained by recording the intensity of the luminophore emission using a scientific grade CCD camera.

As shown in figure 2, implementation of a PSP system requires a luminophore-impregnated, oxygen permeable

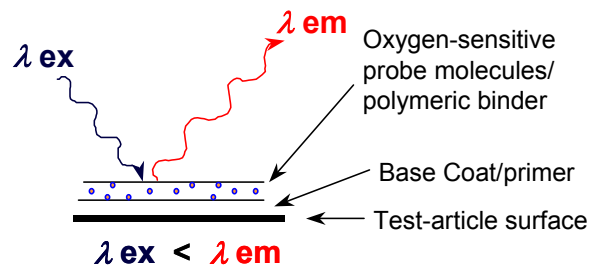


Figure 1: PSP photophysics.

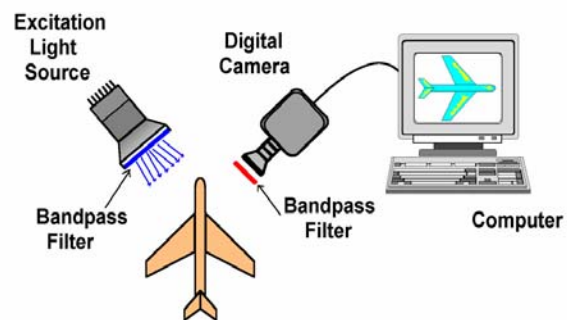
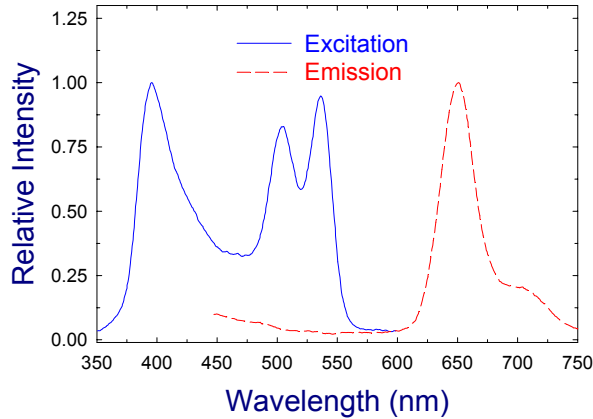
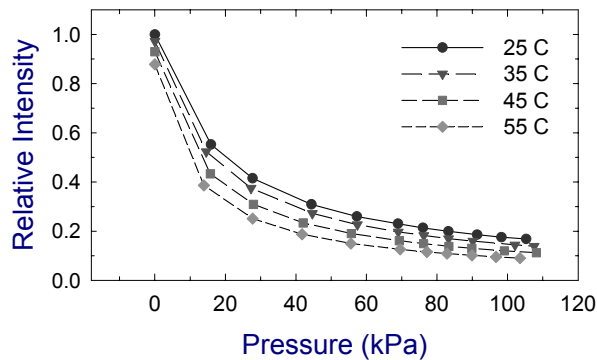


Figure 2: Schematic depicting a generic PSP measurement system.



**Figure 3:** Absorption and emission spectra for Pt(TfPP) luminophore



**Figure 4:** Typical PSP calibration data showing response as a function of pressure and temperature

paint, illumination source(s), scientific-grade CCD camera(s), and optical filters for spectral discrimination between excitation, emission, and background light. Typical absorption and emission spectra for a commonly used luminophore (Pt[TfPP]) are shown in figure 3. These data indicate that illumination of this specific luminophore with light between  $\sim 360 - 540$  nm results in pressure-sensitive emission between  $\sim 620 - 750$  nm. An optical band pass filter centered at the 650 nm emission peak is placed in front of the CCD camera to segregate the pressure-sensitive emission from the illumination and background light. Images of the painted surface are acquired in both wind-off and wind-on conditions for each model configuration (e.g., angle-of-attack) tested. The corresponding wind-off and wind-on images are spatially registered<sup>19</sup> and subsequently ratioed to produce an image whose grayscale intensity is inversely proportional to surface pressure. The intensity maps are then converted into pressure maps by applying either an *a priori* calibration determined using a pressure/temperature-controlled

apparatus in the laboratory, or by applying an *in situ* calibration using a small population of pressure taps<sup>20-30</sup>. Data collected from the pressure taps are typically used to compensate for PSP temperature sensitivity, which is, in most cases, the largest source of error in PSP measurements. Data showing the relationship between PSP response and temperature is shown in figure 4. Multi-luminophore, multi-layer paints that exhibit spectrally unique pressure- and temperature-sensitive emission are currently being developed to eliminate the need for pressure taps<sup>27, 31-32</sup>.

### **On-body: Projection Moiré Interferometry (PMI)**

PMI is a video-based, non-contacting measurement technique capable of obtaining spatially continuous measurements of out-of-plane structural deformations<sup>33</sup>. The technique is well suited to measuring the deformation of aeroelastic vehicle components or aerodynamic control surfaces<sup>34-38</sup>. Measurement of the out-of-plane surface deformation is critical for many shape-change flow control devices, and determining the overall control authority often requires coupled measurements of the surface deformation and on- and off-body flow characteristics. Thus PMI was used in the Unified Instrumentation Test to evaluate its compatibility with the other optical measurement methods used, with the goal of providing the capability to simultaneously measure control surface actuation and aerodynamic reaction.

PMI as applied to measuring wind tunnel model deformation is shown schematically in figure 5. A projection system is used to project a grid of equispaced, parallel lines onto the wind tunnel model surface. Any incoherent light source providing adequate illumination levels can be used for grid line projection, but pulsed laser diodes emitting in the near infrared (IR) are often used for large scale wind tunnel tests. Laser diodes provide the high light intensity levels required for measuring deformations over large fields-of-view, and, by optical filtering, provide the ability to spectrally isolate the PMI system illumination from other light present in the wind tunnel. This enables lights-on facility operation without loss of projected grid line contrast, and the potential for simultaneous operation with other optical measurement techniques. The projector system is typically aligned such that its optical axis is perpendicular to the surface being measured. A Ronchi ruling (a transmissive grating with opaque parallel lines etched at equal spacing and thickness) installed in the projector is the physical element generating the projected grid lines. A CCD camera with a narrow band pass filter matched to

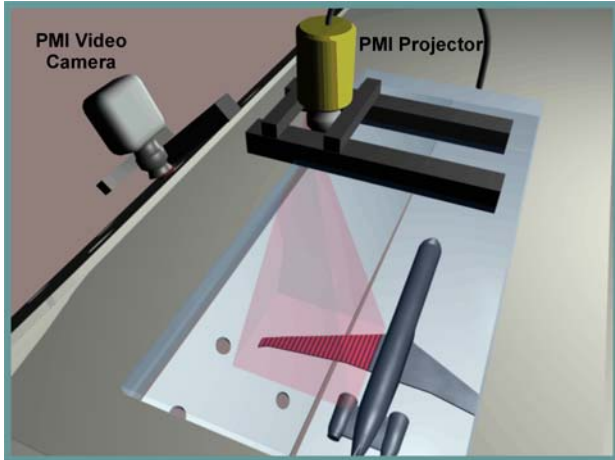


**Figure 5:** Conceptual use of PMI for wind tunnel model deformation measurements

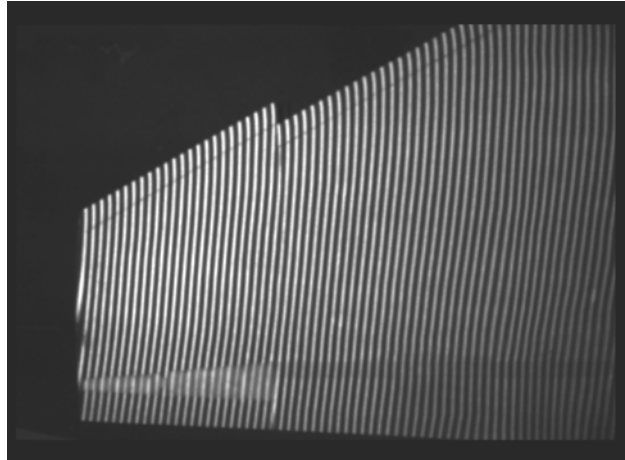


**Figure 6:** Raw PMI data image showing projected grid lines

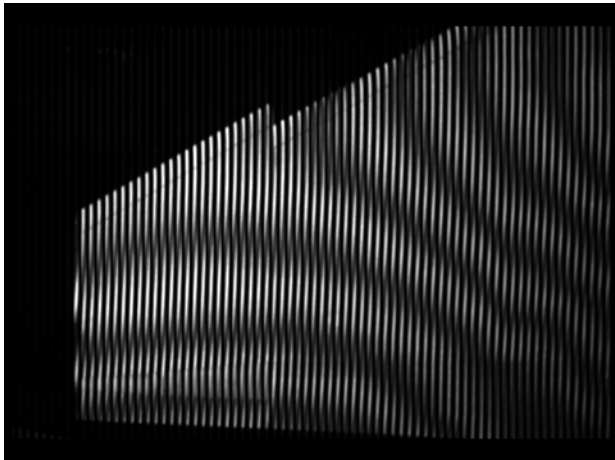


**Figure 7:** Moiré fringes generated by interfering raw PMI data, figure 6, with a computationally generated reference grid

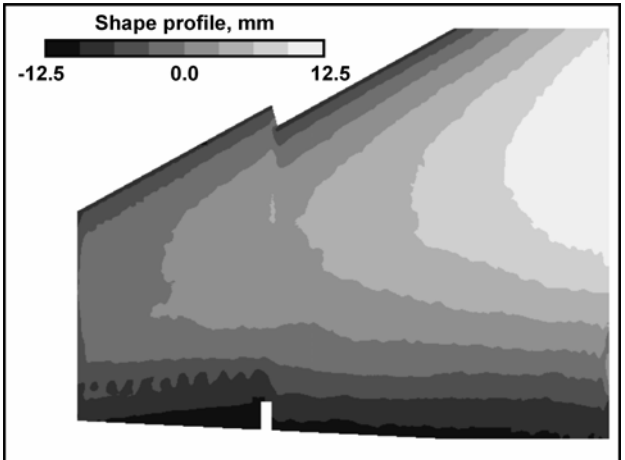


**Figure 8:** PMI-measured airfoil shape data obtained by processing moiré fringe images as in figure 7

the projector illumination wavelength is positioned to view the model at a 30-45° angle inclined from the projector optical axis. The projector and camera must lie within a plane perpendicular to the projected grid lines. Images of the grid lines projected onto the model are acquired in baseline (wind-off) and loaded (wind-on) conditions using a frame grabber installed in a PC-compatible computer. An example PMI raw data image with an approximate 1.2-x 1.2-meter field-of-view is shown in figure 6. Image processing routines are then used to remove camera perspective distortion and interfere the acquired images with a computationally generated reference grid, resulting in interferograms containing moiré fringes, figure 7. These fringe patterns are further processed offline to obtain a quantitative, spatially continuous representation of the model surface shape or

deformation, as shown in figure 8. The PMI system measurement accuracy and resolution are primarily dependent upon the projected grid pitch, video camera field-of-view, optical modulation transfer function, and illumination / observation angles<sup>39</sup>. The deformation measurement accuracy and resolution of the PMI system used to acquire the data shown in figures 6 – 8 was 0.75-mm with 0.5-mm resolution respectively<sup>37</sup>, typical of PMI systems used in other large wind tunnel applications.

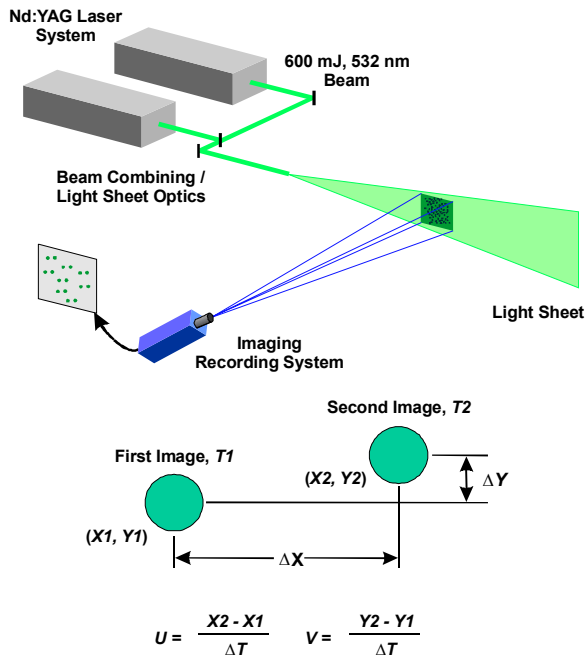


Figure 9: DPIV concept.

### Off-Body: Digital Particle Image Velocimetry (DPIV)

DPIV is a mature method for measuring off-body flow velocity. The technique is based on tracking tracer particles embedded in the flow as they are illuminated by a series of pulsed light sheets. The advent of Particle Image Velocimetry (PIV) in the 1980's, followed by DPIV in the 1990's, has enabled researchers to examine complex off-body flow fields in great detail<sup>40-41</sup>. References 42-45 provide comprehensive reviews of the PIV/DPIV technique.

A generic DPIV system is shown in figure 9. Typical DPIV operation consists of utilizing the beam from a multiple-pulse (e.g., double-pulse) Nd:YAG laser system to form a thin sheet of light which is directed into the flow within the field-of-view of the DPIV camera system. Particles are illuminated by a series of short (nominally 10 nS) pulses of light with a fixed inter-pulse time delay. The recording and laser systems are synchronized such that each camera frame obtains one exposure per laser pulse. These camera frames may be acquired using a frame-straddling camera where one camera captures multiple light sheet pulses on different frames. Conversely, as was the case for the present experiment, multiple cameras may be employed with polarization used to direct the scattered light from particles to the various cameras. Analysis of the

recorded images to extract velocity information consists of segmenting the images into small, square interrogation regions typically no more than 32 – 64 pixels wide. Corresponding interrogation regions from pairs of laser exposures are cross correlated to provide an indication of the two-dimensional particle movement within the plane of the light sheet. Flow velocities are then extracted by dividing the physical measure of the particle movement by the laser pulse separation time.

DPIV was considered a fundamental measurement technique for acquiring off-body velocity measurements during the Unified Instrumentation Test, and provided a standard for accurately defining the off-body flow structure and velocity magnitude. Use of the DPIV system also facilitated exploration of how the other optical measurement techniques interacted with a commonly used off-body velocity measurement method.

### Off-Body: Doppler Global Velocimetry (DGV)

DGV was a second non-intrusive diagnostic used to acquire off-body velocity measurements during the Unified Instrumentation Test. DGV is similar to DPIV in the fact that both methods acquire flow velocity measurements within a plane of laser light. DGV has reduced accuracy compared to DPIV, but can obtain measurements over a larger field-of-view. The inclusion of DGV in the Unified Instrumentation Test was intended to demonstrate two capabilities. The first was to provide an alternative method to measure the off-body flow velocity. The second was to demonstrate the ability of DGV and DPIV to share hardware components, including data acquisition hardware and software, towards constructing a single measurement system capable of acquiring both DGV and DPIV data. The intent of this dual system was to use the large field-of-view velocity measurement capabilities afforded by DGV to determine the overall flow field characteristics, then shift to DPIV and stereo DPIV to “zoom in” on smaller areas of interest in the overall view for detailed measurements.

DGV is capable of measuring the three-component flow velocity within a measurement plane defined by a laser light sheet<sup>46-47</sup>. The key element in the DGV approach is the use of the absorption characteristics of Iodine vapor, figure 10, to determine the absolute optical frequency of Doppler shifted laser light scattered by small particles passing through a laser light sheet. Since the optical frequency of the scattered light is measured directly, the resolution of light scattered from a single particle is not necessary. Further, since optical

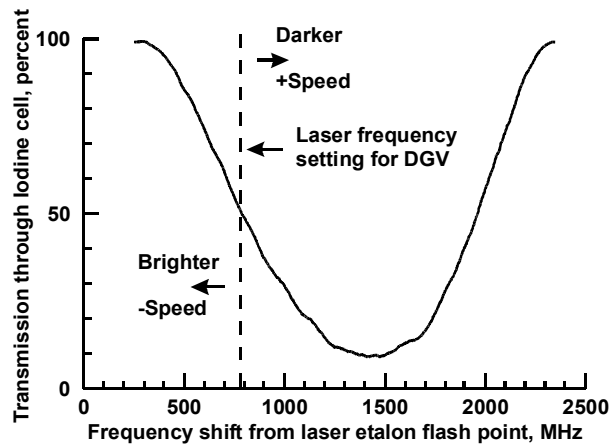


Figure 10: Iodine vapor absorption line transfer function, 514.5 nm

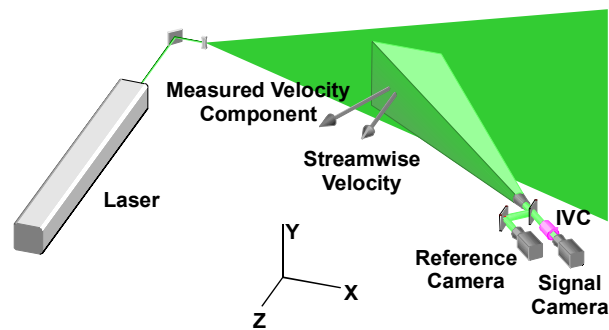


Figure 11: Doppler Global Velocimeter optical configuration.

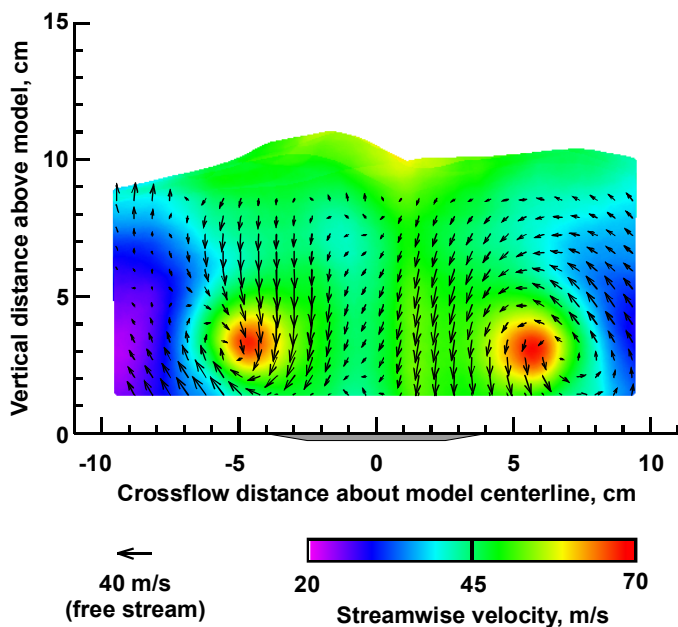


Figure 12: DGV measurements of the vortical flow above a 76-degree delta wing, angle-of-attack = 20.5 degrees, 70-percent chord

heterodyning is not used, multiple particles may coexist in the measurement volume without the complications found in other laser velocimetry techniques. Thus, many very small (<0.2 micron) particles can be used to illuminate a laser light sheet and velocity maps can be determined using standard video cameras.

Figure 11 shows the DGV configuration for measurement of a single flow velocity component. A three-component DGV system consists of a single frequency laser, either Argon ion<sup>48-51</sup> or frequency-doubled Nd:YAG<sup>52-59</sup>, three receiver systems each consisting of two video cameras and an Iodine vapor cell, and a laser frequency monitor – a fourth receiver system used to monitor the optical frequency of the laser. The laser beam is expanded into a light sheet and oriented to the desired measurement plane. Each receiver system is placed about the light sheet to yield the maximum common viewing area with each out-of-plane angle set greater than 30-degrees to minimize viewing pixel overlap errors. The receivers are also set to positions that will yield component velocity vectors that are greater than 45-degrees from each other. The laser optical frequency is then tuned to a point midway along the side of the absorption line, figure 10. When small particles pass through the light sheet, the scattered laser light is Doppler shifted based on their direction and velocity. When a portion of this scattered light is collected and directed through the Iodine vapor, some of the light energy will be absorbed by the vapor. The amount of light energy reduction will be greater (or less, depending on the direction of the Doppler shift) than that lost if a portion of the original laser beam were directed through the cell. Since the optical power passing through the Iodine vapor is also dependent on the particle number density, particle size, and laser intensity profile, a second or reference video camera is used to obtain a map of the collected scattered light intensities. A beam splitter is placed in front of the Iodine vapor cell to direct a portion of the collected scattered light toward the reference camera via a mirror, figure 11. This configuration is used to maintain the same optical axis and image orientation for the two cameras. Normalizing the signal image by this reference image yields the desired velocity-dependent transfer function imposed by the Iodine vapor. The ratio-to-frequency calibration of each Iodine vapor cell and Doppler shift equation are then used to determine the velocity of the flow passing through the light sheet at every pixel viewing point. An example velocity map of the flow above a delta wing is shown in figure 12.

## THE UNIFIED INSTRUMENTATION TEST - GENERAL TESTING PHILOSOPHY

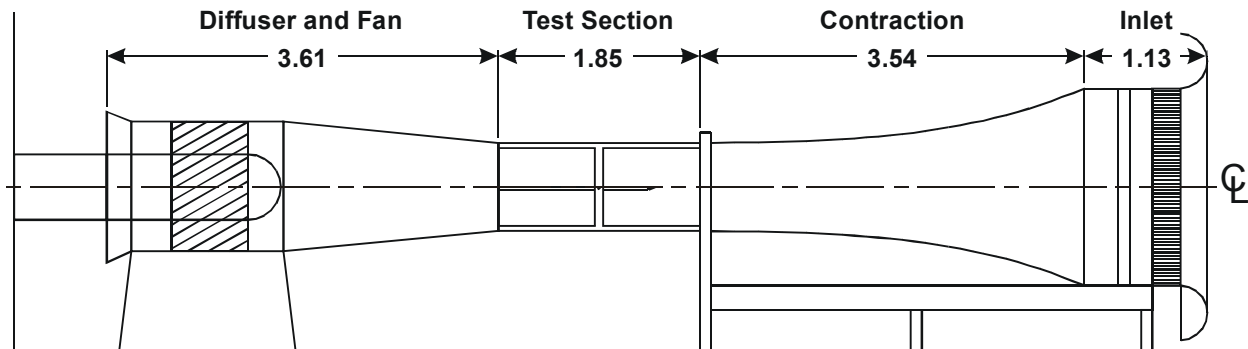
The Unified Instrumentation Test was conducted purely as an instrument development exercise to (a) identify and solve compatibility issues among the techniques used that would inhibit their simultaneous application in a wind tunnel, and (b) demonstrate that simultaneous use of advanced optical instrumentation techniques is feasible for increasing tunnel efficiency and identifying control surface actuation / aerodynamic reaction phenomena. The test was *not* conducted to study flow physics, or to demonstrate the acquisition of measurements at the highest levels of quantitative accuracy. Although measurement accuracy was important, the most important conclusions to be reached involved understanding how each instrumentation system interacted with the others, which systems could be used together on a non-interference basis, and what changes could be made to facilitate the future development and application of instrumentation in a unified testing scenario. Incorporating these lessons learned into the development paths of each instrumentation system highlighted in this paper will significantly ease system integration issues for future tests requiring the simultaneous use of multiple measurement techniques.

## TESTING FACILITIES AND WIND TUNNEL MODEL

The Unified Instrumentation Test was conducted in the LaRC Subsonic Basic Research Tunnel (SBRT), shown in figures 13 – 14. The SBRT is a subsonic, open-return wind tunnel with a 0.56-x 0.81-x 1.86-meter (w-x h-x l) test section. The test section is equally divided into upstream and downstream bays with removable

sidewalls to facilitate model installation and test section access. The upstream bay ceiling and walls are float glass and provided sufficient optical access for viewing the model. One of the rear bay sidewalls was plexiglass with a 75-mm diameter quartz glass insert for transmission of the high power laser beams used for flow visualization, DPIV, and DGV. The tunnel operates at atmospheric pressure and provides free stream velocities up to ~50 m/s. The SBRT is housed in a room that is barely large enough for the facility, yielding minimal space for additional instrumentation.

The model used during the test was a flat plate with a hinged leading edge, shown in figure 15. This configuration was chosen specifically for instrument development purposes as opposed to a model with classical aerodynamic shape. Careful consideration was given to designing a model that generated structural and flow characteristics that could be resolved by each of the instrumentation techniques used. Additionally, the flat plate design allowed for the use of an existing AMA panel that was populated with numerous pressure taps, which could be used as reference points for both the AMA and PSP measurements. The flat plate leading edge angle (LEA) was adjustable from  $-12^\circ$  to  $+12^\circ$ , causing the creation of a flow separation bubble at positive inclination angles. The flow separation bubble provided an interesting flow field for DPIV and DGV off-body velocity measurements, and a well defined reattachment line that could be detected with on-body PSP and AMA. The adjustable leading edge also provided a variable-shape surface facilitating the application of PMI for measurement of the LEA. Thus the separated flow region (on-body and off-body) downstream of the model leading edge was the primary area of concentration for all measurement techniques used.



Dimensions in meters

**Figure 13:** Schematic of the NASA Langley Subsonic Basic Research Tunnel (SBRT).



**Figure 14:** Photograph of the SBRT.

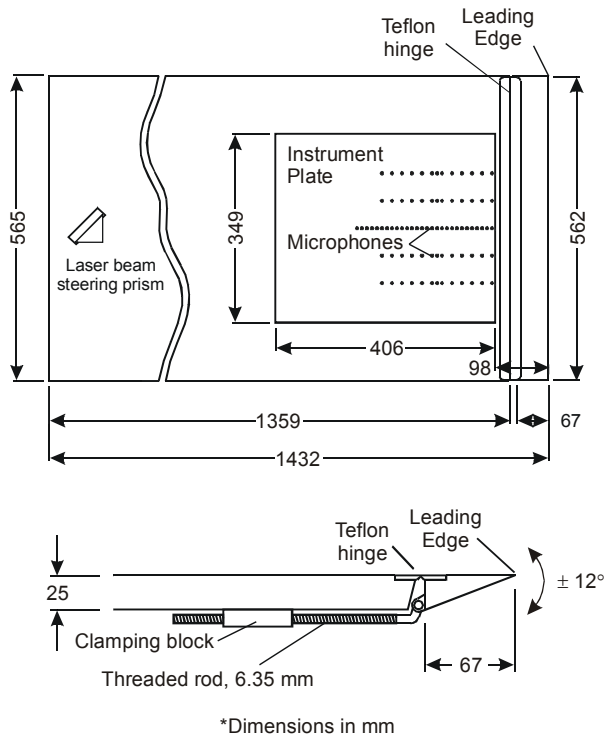


**Figure 15:** Flat plate model with hinged leading edge.

## MEASUREMENT TECHNIQUE IMPLEMENTATION

### VF Implementation

A VF model of the SBRT facility was constructed far in advance of the actual tunnel entry date. The VF model was used extensively for pretest planning and determining how to adequately position all of the required instrument components about the SBRT test

section. The greatest challenge was to determine how to mount each optical component in a position as close to optimal as possible, within the spatial constraints imposed by the facility, without interfering with the other instrumentation components. Modeling the entire experiment, including the tunnel, its surroundings, test configuration, and all of the instrument hardware in a virtual environment was the only way to accomplish this task without consuming weeks of additional tunnel occupancy time.

A CAD model of the SBRT facility was required to establish the basis of the VF model. Blueprints of the 1940's vintage facility could not be found, so physical dimensions of the facility were recorded and manually input into the VF software. This produced a fully detailed model of the tunnel and surrounding room, including windows, ceiling rafters, tunnel drive motor, etc. The resulting virtual rendition of the SBRT facility is shown in figure 16. The wind tunnel model used for the Unified Instrumentation Test was also integrated into the VF model, using dimensions extracted from the drawings used for hardware fabrication. Finally, each hardware component for all of the instrumentation systems used during the Unified Instrumentation Test was geometrically modeled. Optical receiver systems, such as the PSP and PMI video cameras and DPIV/DGV receivers, were modeled using lensing and optical ray tracing capabilities intrinsic to the VF software. This provided the ability for the researcher to visualize what each camera system would be imaging at any prospective mounting location. The PSP and PMI illumination sources were modeled as spotlights to investigate whether adequate illumination could be achieved on the model surface, or whether tunnel structure in the illumination path would cause shadowing. The DPIV/DGV laser light sheet was also modeled to predict the divergence required to adequately illuminate the separated flow region behind the model leading edge, and to define the plane of measurement for DPIV and DGV.

The nominal locations for the PMI and PSP hardware were determined with relative ease. Both instrumentation systems required clear optical access to the wind tunnel model top surface. Thus the virtual PMI and PSP cameras and illumination sources were situated above the test section ceiling and aligned to view the model top surface, figures 17 – 18. The virtual components were then iteratively positioned until it was assured that the real components could coexist, albeit in very close proximity, without obscuring each other's field-of-view.

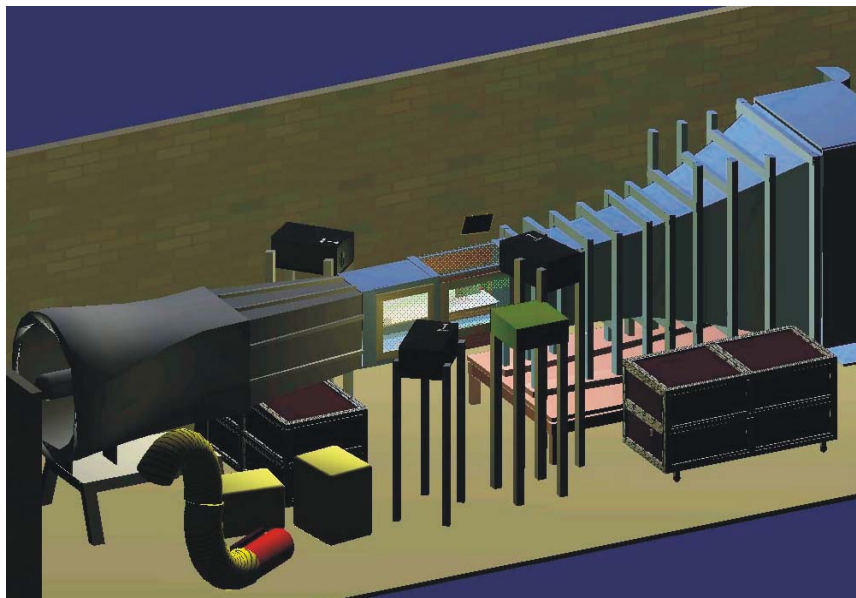


Figure 16: Virtual rendition of the SBRT facility.

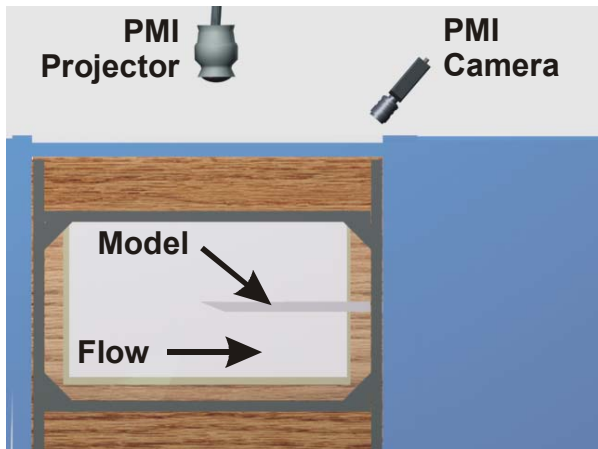


Figure 17: PMI projector and camera placement.

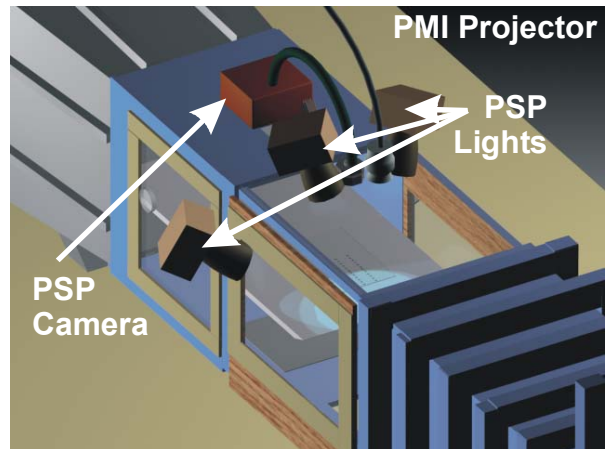


Figure 18: PSP camera and light placement.

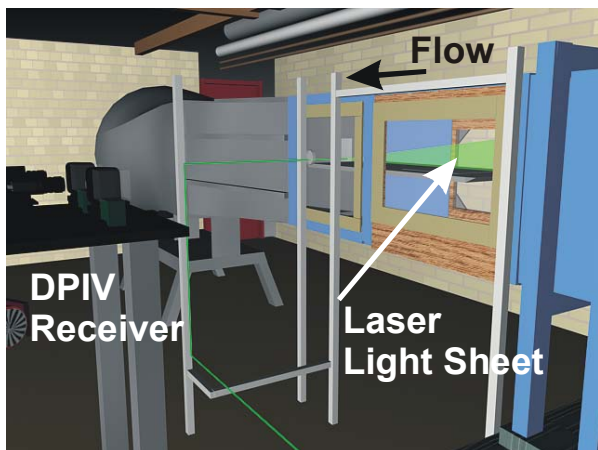


Figure 19: 2D DPIV setup showing camera platform and laser light sheet location.

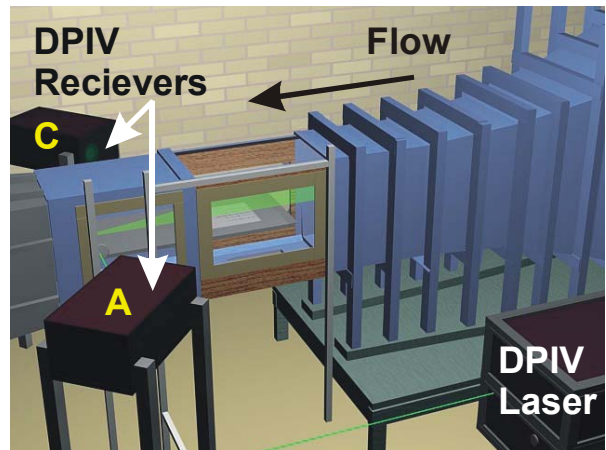
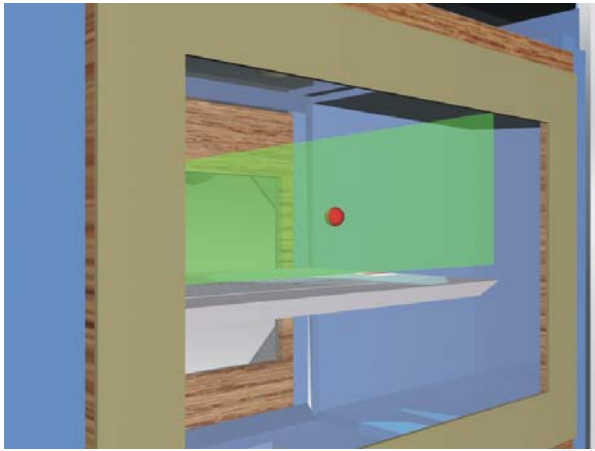


Figure 20: Optical receiver locations for stereo DPIV and two of the DGV receivers, denoted as components "A" and "C".



**Figure 21:** Simulated camera view from DPIV/DGV receiver location "A". Floating ball is for targeting.



**Figure 22:** Simulated camera view from DPIV/DGV receiver location "C".

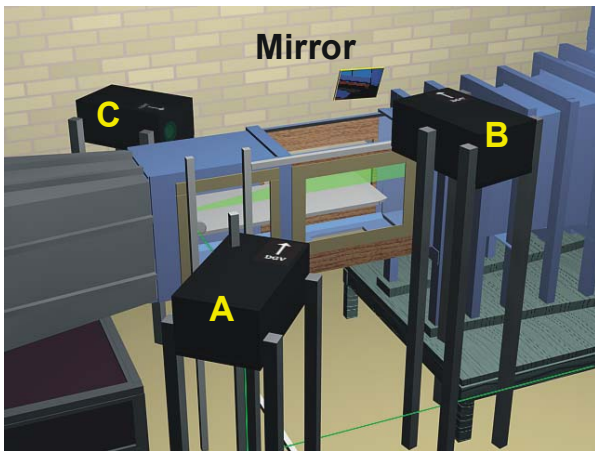


**Figure 23:** Receiver system locations for 3-component DGV measurements.

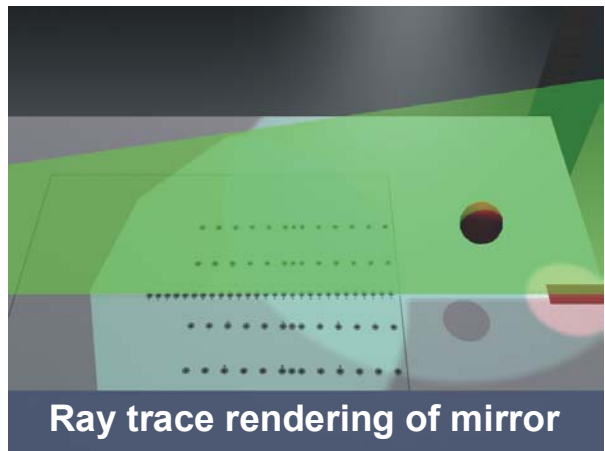


**Figure 24:** Simulated camera view from DGV receiver location "B".

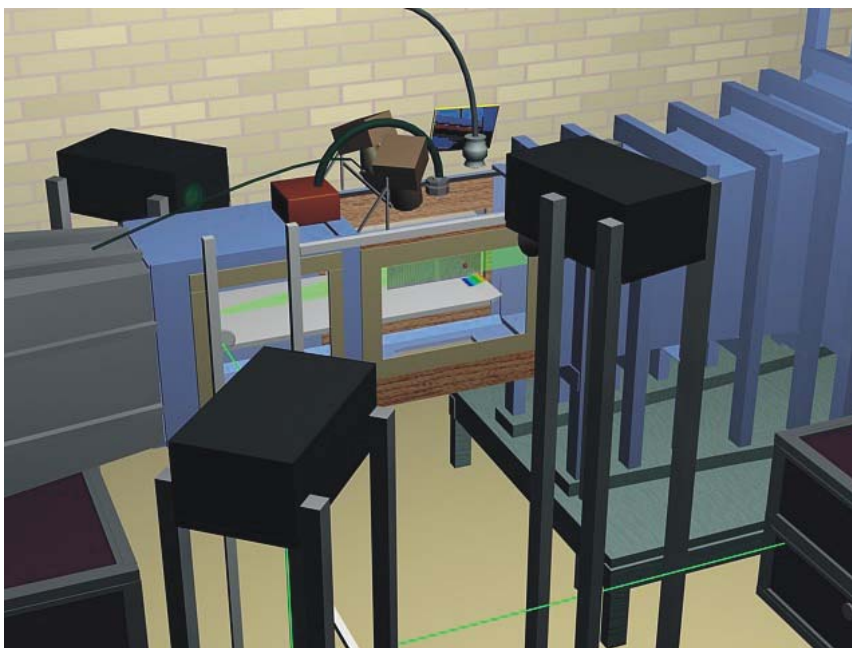


**Figure 25:** Final hardware configuration for unified instrumentation testing.

The locations of the DPIV receivers for acquiring 2-component velocity measurements in the separated flow region were determined next. The receivers were positioned at the nominal height of the flow separation bubble and aligned to view the DPIV light sheet perpendicularly, figure 19. Since these components were positioned on the side of the tunnel, there was no possibility that they would interfere with the PMI and PSP hardware. Additionally, there was no concern that the DPIV hardware, when configured in this manner, would interfere with the DGV hardware since the two instruments would not be operated simultaneously.

Determining the locations of the stereo DPIV and DGV hardware for 3-component velocity vector measurements was much more challenging. The DGV system imposed the most stringent requirements for locating the optical receiver components for two reasons:

1. The velocity vector component measured by each receiver system is dependent on the illumination and observation angles, and
2. It is desired to maintain at least a 45° separation angle between measured velocity components to minimize errors that may propagate through the coordinate transform required to convert the measured velocities to the conventional streamwise-vertical-crossflow reference frame.

Additionally, it was desired to position the stereo DPIV receivers and two of the DGV receivers at the same locations to explore the ability to acquire DGV and stereo DPIV measurements with common receiver systems. Thus the positioning requirements for the stereo DPIV receivers had to be considered concurrently. Following a substantial amount of trial-and-error positioning of the virtual hardware components, it was determined that the best compromise for the position of the two DPIV / DGV receivers was downstream of the model, symmetric about the light sheet, oriented upstream to view the separated flow region behind the wind tunnel model leading edge, as shown in figure 20. The simulated camera views from these positions are shown in figures 21 – 22.

With two of the DGV receiver positions now fixed, the location of the third receiver had to be determined to satisfy the positioning criteria noted above. Locating the two receivers at positions suitable for stereo DPIV provided the DGV system with sufficient sensitivity to resolve flow velocities in the streamwise and crossflow

directions, but complete insensitivity to the vertical velocity component. Sensitivity to the vertical component could only be obtained if the third DGV receiver was aligned to view the light sheet at an oblique downward angle. Unfortunately this was not directly possible because of the minimal clearance above the test section, coupled with the existence of the PMI and PSP hardware. The VF model was used to determine that the third DGV receiver could be mounted as high as possible on the right side of the tunnel and oriented to look cross stream to a downward-tilted mirror on the left side of the tunnel, figure 23. The mirror was angled so the DGV receiver could image the light sheet appropriately, figure 24, achieving the needed sensitivity to the vertical velocity component. The final DGV / PMI / PSP configuration for unified testing is shown in figure 25.

### **On-body: AMA Implementation**

An instrumented plate (hereafter referred to as an I-plate) that contained the microphones comprising the AMA was installed in the upper surface of the model near the leading edge, figure 26. This enabled the acquisition of unsteady pressure measurements in the vicinity of flow separation and reattachment. The particular I-plate used for this test was previously employed to characterize the separated flow above a backward step model constructed by Michigan State University<sup>5</sup> and was modified for insertion into the unified instrumentation model. The plate was populated with 80 flush-mounted electret microphones acting as hydrodynamic pressure sensors. Figure 27 illustrates the location of these sensors on the I-plate. The array consisted of 28 microphones mounted along the centerline of the plate with two rows each containing 13 microphones located on either side of the centerline. A total of 40 pressure taps were also positioned on the plate - 28 taps located parallel to the centerline row of microphones and four other rows each containing 3 taps. All taps were offset from their corresponding microphones by 5.4 mm. A 48-channel electronically scanned, differential pressure module (ESP system) with a maximum range of 10 inches of H<sub>2</sub>O was used to sample each of the pressure taps. Acquisition of pressure tap data was not synchronized with the other instrumentation used during the test, primarily because of complications that arose when attempting to remotely trigger the previously existing ESP data acquisition software. Instead, pressure tap data were acquired at the beginning and end of the data acquisition sequences for the other techniques. This method of data acquisition was deemed acceptable



**Figure 26:** I-plate painted with PSP and mounted in SBRT Tunnel. Unpainted stripes correspond to rows of microphones and pressure taps.

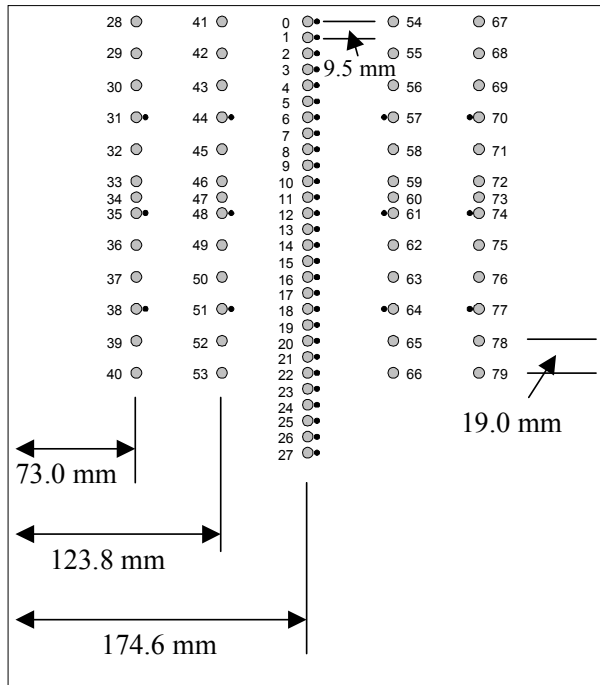


**Figure 27:** Location of static taps and microphones on the I-plate. Large diameter circles represent microphones, small diameter circles represent taps.

since the taps provided time averaged surface pressure data, and the data showed no noticeable change from the beginning to the end of a data acquisition sequence.

A 64-channel signal conditioning system was used to provide gain and anti-alias filtering of signals acquired from the microphones in the I-plate. The conditioned signals were digitized using a 64-channel multiplexed acquisition card contained in a PC. Each

acquisition channel was sampled at 6 kHz, yielding an analog bandwidth of 3 kHz per channel, well above the estimated spectral bandwidth of 1 kHz expected in the separated flow field sampled by the AMA. During data acquisition, data from 64 microphones selected from the 80 on the I-plate were acquired simultaneously, and the AMA data acquisition was fully synchronized with the other measurement techniques. AMA data were acquired at a 6 kHz per channel sampling rate for a 25-second record length, generating 150,000 samples per microphone for each condition tested.

**Tap Analysis:** Analysis of the surface pressure tap data consisted primarily of computation of the pressure coefficient as a function of the distance along the model centerline. The pressure coefficient was determined using the commonly applied formula

$$C_p = \frac{p_s - p_r}{\frac{1}{2} \rho U_\infty^2} \quad (1)$$

where  $p_s$  represents the surface pressure at a tap and  $p_r$  is a reference pressure measured at the leading edge of the test section. A normalized formulation of the pressure coefficient<sup>60</sup> was used in plotting results:

$$C_p^* = \frac{C_p - C_{p,min}}{1 - C_{p,min}} \quad (2)$$

where  $C_{p,min}$  is the minimum  $C_p$  along the model centerline.

**Microphone Analysis:** Analysis of the dynamic surface pressure data obtained from the AMA consisted of both time-domain analysis to obtain RMS pressure distributions and frequency-domain analysis using block-averaged statistical signal processing to obtain auto spectra, cross spectra magnitude and phase, and inter-channel coherence. The various forms of data analysis are described below.

**Time-Domain Analysis:** The primary time-domain analysis conducted on the acquired microphone data consisted of computation of the root-mean-squared (RMS) pressure fluctuations at each microphone. This was done after converting the raw data to engineering units (Pascals) using sensitivity data obtained from microphone calibrations over a frequency range of 1 to 3 kHz. The RMS values were computed via

$$V_{i,RMS} = \sqrt{\frac{\sum_{k=1,n} (p_k - \bar{p})^2}{n-1}} \quad (3)$$

where  $p_k$  is the  $k^{\text{th}}$  pressure sample from an  $n$ -sized ensemble acquired for microphone  $\#i$ . The RMS pressure distribution along the centerline of the model is an excellent indicator of flow reattachment. As described by Hudy in reference 5, the commonly held view is that the RMS pressure distribution is dominated by the interaction of shear-layer vortical structures generated by the separation bubble with the surface of the model. As these structures convect downstream, they grow in size and intensity and move closer to the surface of the model. At the point of flow reattachment, the interaction of the structures with the surface of the model reaches a maximum.

**Frequency-Domain Analysis:** The primary frequency-domain analysis conducted on the acquired microphone data consisted of the computation of an  $M$  by  $M$  cross spectral matrix on the centerline row of microphones, where  $M$  is the total number of microphones on the array centerline (in this case, 28). The formation of the individual matrix elements was achieved through the use of Fast Fourier Transforms (FFT), performed after conversion of the raw data to engineering units (Pascal's). Each channel of engineering unit data was segmented into a series of non-overlapping blocks each containing 1024 samples, yielding a frequency resolution of 5.8 Hz for the 6 kHz acquisition sampling rate. Using a Hamming window, each of these blocks of data was Fourier transformed into the frequency domain. The individual upper triangular matrix elements plus the diagonal (representing auto spectra for each array microphone) were formed by computing the corresponding block-averaged cross spectra from the frequency data using

$$\hat{G} = \begin{bmatrix} G_{11} & G_{12} & \dots & G_{1M} \\ & G_{22} & & \vdots \\ & & \ddots & \vdots \\ & & & G_{MM} \end{bmatrix} \quad (4a)$$

with

$$G_{ij}(f) = \frac{1}{NW_s} \sum_{k=1}^N [X_{ik}^*(f)X_{jk}(f)] \quad (4b)$$

where  $W_s$  is the data window weighting constant,  $N$  is the number of blocks of data, and  $X$  represents an FFT data block. The lower triangular elements of the matrix were formed by taking the complex conjugates of the upper triangular elements (allowed because the cross spectral matrix is Hermitian). Individual spectra were extracted from the cross spectral matrix (auto spectra from diagonal entries, cross spectra from non-diagonal) and displayed as sound pressure level (SPL) relative to 20  $\mu$ Pascals versus frequency. The ordinary inter-channel coherence was computed for combinations of off-diagonal entries in the cross spectral matrix via

$$\gamma_{ij}^2 = \frac{|G_{ij}(f)|^2}{G_{ii}(f)G_{jj}(f)} \quad (5)$$

The computation of the cross spectral matrix and extraction of auto spectra, cross spectra, and coherence is very similar to processing performed by the authors for aeroacoustic directional microphone arrays.

### **On-body: PSP Implementation**

PSP was used to obtain measurements of the steady state pressure distribution on the I-plate surface, figure 26. By coupling the PSP measurements with those obtained with the AMA, both the steady and unsteady pressure distribution on the I-plate surface could be fully determined. Obtaining PSP measurements over this region-of-interest also provided the capability to correlate the surface pressure distribution with the off-body velocity measurements obtained in the separated flow region above the model, and examine compatibility issues with PMI and the off-body velocity measurement techniques. As a matter of practicality, pressure taps already incorporated into the I-plate served as reference pressures for the PSP data.

The PSP system optical components consisted of a single 16-bit scientific grade CCD camera and two 102-mm diameter light emitting diode (LED) arrays. The PSP camera was mounted above the tunnel test section ceiling on the tunnel centerline, slightly downstream of the I-plate geometric center, and aligned to view the I-plate. The LED arrays were also mounted above the test section ceiling near the side walls, and

provided broadband blue illumination centered at 464 nm for paint excitation. The camera was equipped with a  $650 \pm 40$  nm optical band pass filter and an IR-blocking filter to spectrally isolate the PSP emission from the PSP illumination and laser light used by the remaining optical measurement techniques. A fiber optic video interface was used to transmit PSP data images back to the tunnel control room, where they were acquired and stored using a frame grabber installed in a PC-compatible computer.

The PSP was a ruthenium bathophenanthroline (RuB)-doped sol-gel formulation on a trifluoroethylmethacrylate copolymer (FEM) base coat. This paint composition was developed specifically for low-speed pressure sensitivity and dynamic response exceeding 1 kHz. The paint has high pressure sensitivity exceeding 0.7%/kPa, relatively low temperature sensitivity at  $\sim 1.2\%/^{\circ}\text{C}$ , and excellent compatibility with blue LED illumination. The paint was applied to the I-plate *in-situ*, while the I-plate and model were installed in the tunnel test section. The I-plate microphones and pressure taps were masked prior to PSP application.

Continuous-wave (CW) LED illumination was used during PSP data acquisition. Sixteen images, each having a 1-second exposure time, were acquired for each tunnel condition. The 16-independent images were then averaged to improve the measurement signal-to-noise ratio and subsequently processed using the Greenboot® PSP image processing software<sup>19</sup>. The PSP results were then converted to pressure (or pressure coefficient,  $C_p$ ) by an *in situ* calibration using 25 of the 28 centerline taps on the I-plate. PSP data were acquired both independently and unified with the AMA, PMI, DPIV, and DGV. PSP data were acquired from a single paint application with negligible decreases in signal for a period exceeding one month, demonstrating the robustness of this paint formulation to low- and high-impact damage, sedimentation of tunnel debris, photodegradation, and contamination by off-body velocimetry seeding.

#### **On-body: PMI Implementation**

PMI was used to measure the model leading edge deflection angle. The leading edge, constructed of solid aluminum, was not expected to exhibit any aeroelastic deformation and therefore provided a relatively uninteresting test article for PMI measurements. The predominant goal of exploring the PMI system compatibility with the other measurement techniques, however, could still be achieved using this approach.

The PMI system was configured to measure the leading edge deflection in an approximate 125-x 125-mm region-of-interest at the front of the model, slightly off centerline. The PMI system hardware was mounted above the SBRT test section and aligned to view the model top surface through the float glass test section ceiling. As shown in figures 17 – 18, VF models of the experimental setup were used to strategically position the PMI system hardware components to achieve cohabitation with the PSP equipment.

A laser diode bar emitting 795 nm was used as the PMI system illumination source. The laser light was fiber optically coupled from the tunnel control room to the PMI projector head installed above the test section. The projector head optical axis was aligned perpendicular to the model top surface, and a 10 line pairs/mm Ronchi ruling was installed in the projector to generate the grid pattern projected onto the leading edge. The leading edge top surface was painted with a flat white PSP primer to provide a diffuse scattering surface for PMI measurements.

The PMI video camera was a standard analog RS-170 compatible CCD camera with 768-x 480-pixel resolution. The camera was mounted downstream of the projector head, angled approximately  $40^{\circ}$  upstream to view the leading edge. A  $795 \pm 5$  nm optical band pass filter was mounted to the PMI camera lens to distinguish the PMI system laser light from other sources of illumination for the remaining optical measurement techniques. The analog video stream produced by the camera was transmitted to the tunnel control room via a video fiber optic interface, and subsequently digitized using a frame grabber installed in a PC-compatible computer. Twenty PMI data images were acquired for each tunnel and model condition tested. The twenty independent images were then averaged to minimize noise present in the video signal and processed off-line to determine the leading edge deflection angle.

#### **Off-body: DPIV and DGV Implementation**

DPIV and DGV were both used to measure the off-body flow velocity in the separated flow region above the I-plate. Although DPIV and DGV cannot be operated simultaneously because of differing operational requirements and receiver configurations, there are numerous areas of commonality that can be exploited towards construction of a single system capable of acquiring both DPIV and DGV measurements. Therefore, in addition to exploring

compatibility with PSP and PMI, one of the primary goals of the off-body measurements portion of the Unified Instrumentation Test was to determine the extent of commonality that could be achieved between the DGV and DPIV hardware.

DPIV and DGV are both typically based on the use of pulsed, frequency doubled Nd:YAG lasers operating at 532 nm wavelength. DGV requires a single-frequency laser whereas DPIV requires either a double-pulse laser or two separate single-pulse lasers. A combined DGV/DPIV laser system could be formed by using one single frequency Nd:YAG laser (for DGV) and one non-injected broadband Nd:YAG laser (for DPIV) in tandem. Many of the other DPIV and DGV components have common requirements and perform similar functions. For example, the DPIV and DGV systems were configured to place potentially common components at the same locations. The same tunnel seeding system was used for both techniques. Common light sheet generation optics were used by both DPIV and DGV to create the light sheet defining the off-body velocity measurement plane. Additionally, the receiver systems were engineered to require only modest changes to the optical configurations to accommodate both techniques. These and additional areas of commonality are described in greater detail below, followed by sections addressing specific aspects of the DPIV and DGV implementations.

Tunnel Off-Body Seeding System: A commercially available smoke generator was used to provide uniform flow seeding for off-body velocity measurements above the I-plate. The smoke produced by the generator was introduced into the facility by entraining it in the flow at the tunnel intake. The smoke generator consisted of a shearing atomizer feeding a vaporization / condensation section. The smoke fluid was pharmaceutical grade mineral oil. The generator produced a cloud of smoke that could be varied in density by adjusting the atomizer supply pressure. Smoke densities ranging from a wisp to an amount of smoke that would fill the SBRT room within a few minutes were possible. Thus the seed particle density requirements for both DPIV and DGV could be easily met. The smoke particle size ranged from 0.2 to 0.4  $\mu\text{m}$ , measured using a particle size analyzer. This is significantly smaller and more uniform than the 0.4 to 20  $\mu\text{m}$  diameter particles produced by propylene glycol-based theatrical foggers that are often used for DPIV and DGV measurements. Even though the particles were small, they scattered enough light to be imaged by DPIV receivers. The resulting DPIV images contained sufficient particle image pairs to establish an

accurate cross-correlation, and thus velocity vector, within each interrogation region. The particle image diameter was consistent among all particles in the image, indicating good smoke particle size uniformity.

Laser Light Sheet Generation: DPIV and DGV measurements were desired above the I-plate in a vertical plane along the tunnel centerline. The laser light sheet defining this measurement plane was formed by a series of mirrors and lenses that shaped the circular beam from the frequency-doubled Nd:YAG lasers into a sheet approximately 0.3 m in height and 0.5 mm thick throughout the measurement area. The transmission optics are shown in figures 28 – 29. The light sheet illuminated by flow seeding is shown in figure 30. The growing sheet was injected into the tunnel downstream of the model trailing edge and turned upstream using a right-angle prism. Although the single-frequency, frequency-doubled Nd:YAG laser used for DGV could have been one of the two DPIV lasers, separate systems were used since the lasers were of significantly different powers. The DPIV lasers and the DGV laser were placed upstream and downstream respectively from the light sheet forming optics. Thus the laser systems could be switched by the insertion/retraction of a single mirror.



**Figure 28:** DGV laser light sheet generation optics.

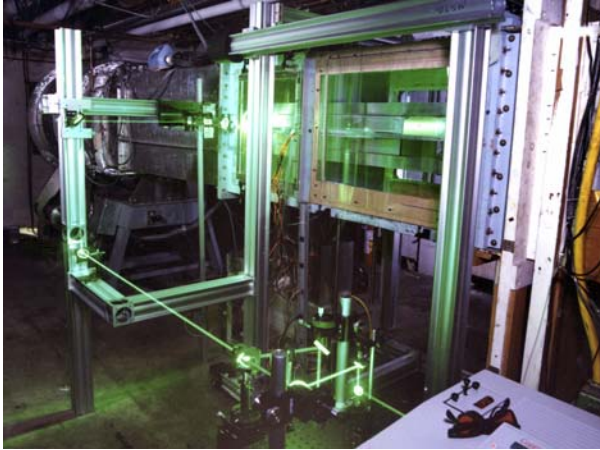


**Figure 29:** DPIV laser light sheet generation optics.

Timing Synchronization System: A custom synchronization and control circuit was constructed to synchronize the DPIV / stereo DPIV and DGV laser(s), cameras and frame grabbers to insure simultaneous operation of the components. The circuit was designed to control up to two lasers and up to eight camera / frame grabber systems. The circuit also monitored the Iodine vapor cell temperatures during DGV applications. In addition this device provided the synchronization signals to begin acquisition for PMI and the AMA.

Data Acquisition System: The DPIV/DGV data acquisition system consisted of a PC-class computer cluster with two frame grabber boards installed in each slave computer (2 for DPIV and 4 for DGV). A master computer was used to provide the user interface and the primary control for the slave computers and synchronization electronics. This data acquisition system, including the data acquisition software, was originally developed for DGV applications. Hardware and software upgrades were then added to the original system to accommodate the high resolution video cameras used for DPIV. Following the upgrades, the system could be used for either DGV or DPIV data acquisition.

Imaging System: The imaging systems for DPIV and DGV were based on the use of two 1300-x 1030-pixel progressive scan CCD cameras that imaged the seeded flow through a beam splitter. The receiver system components used for DPIV are shown in figure 31. The beam splitter used for DPIV applications was a 50.8-mm depolarizing cube. The output beam polarizations of the DPIV lasers were aligned to be orthogonal, such that light emitted during the first laser pulse was S-



**Figure 30:** Laser light sheet flow visualization of the separated flow above the I-plate.

polarized, and light emitted during the second laser pulse was P-polarized. The depolarizing cube was used to direct the particle-scattered light from the first laser pulse to one camera, and the scattered light from the second laser pulse to the other camera. The DGV receiver systems used a non-polarizing beam splitter plate with a 60/40 percent split ratio. An iodine vapor cell was installed between the splitter plate and *signal* camera in the optical path receiving the 60% of the split light. The additional light passed to the iodine cell by the beam splitter helped compensate for optical reflection losses and attenuation through the iodine cell. The remaining 40% of the split light was directed unabated to the *reference* camera.

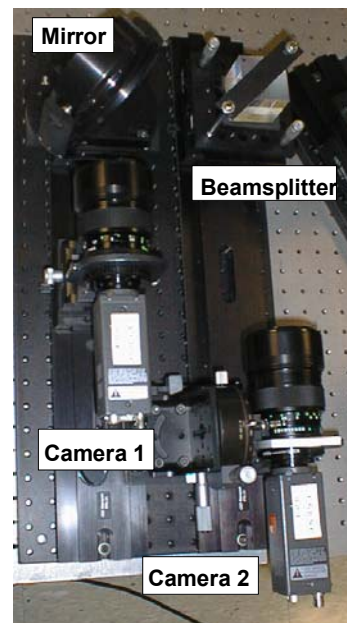


**Figure 31:** Photograph of DPIV image recording system receiver configuration.



**Figure 32:** Two-Component DPIV image recording system. Two receiver systems are placed side-by-side to increase overall DPIV field-of-view.

The DGV receiver assemblies were fully enclosed to protect the optics from the tunnel seeding, provide shielding from extraneous laser light, and to maintain a stable operating environment. The receiver packages were thermally controlled using self-contained heating and air conditioning systems to minimize drift of the iodine vapor absorption characteristics. The DPIV receivers were not enclosed for this study simply for convenience in performing camera alignment adjustments.

The cameras were electronically shuttered to 1/10,000 second for both DPIV and DGV operation. The laser/camera timing was adjusted such that the 10 nS Nd:YAG laser pulse occurred within the camera open shutter time. The minimal exposure time, coupled with the high energy Nd:YAG illumination, ensured that the collected particle scattered light intensity was much greater than other sources of background light, including the PSP illumination and emission. IR-blocking filters were installed in each camera to provide additional extinction of the PMI system laser light. The analog output from the video cameras was transmitted to the tunnel control room via RG-59 coax cable and digitized at 8-bits.

DPIV System Specifics: Two different receiver location geometries were used for DPIV during the Unified Instruments Test. The first enabled measurement of the 2-component flow velocity vector (streamwise, vertical) within the plane of the laser light sheet with optimal accuracy. The second configuration provided stereo views of the light sheet, yielding 3-component flow velocity vector (streamwise, vertical, crossflow) measurements. Two independent DPIV

receiver systems, totaling 4 cameras, were used in both phases of the DPIV investigations.

The DPIV receiver optical configuration used for acquiring the 2-component velocity measurements is shown in figure 32. Although 2-component DPIV measurements can be obtained using a single pair of cameras, two receiver systems were used to expand the DPIV system field-of-view. The two receiver systems were arranged side-by-side and aligned such that their optical axes were perpendicular to the laser light sheet. The use of 135-mm f/2 single-lens-reflex (SLR) lenses on each camera resulted in an 80-x 200-mm (h-x w) combined field-of-view at an approximate 1.5 meter standoff distance. Unfortunately, this field-of-view was not large enough to measure the flow velocity over the full length of the I-plate. Therefore DPIV data was acquired for each test condition with the receiver system shown in figure 14 located at two streamwise stations. The vector maps acquired from the upstream and downstream stations were subsequently merged to generate the off-body flow velocity map for an overall 80-x 400-mm field-of-view from the model leading edge to the I-plate trailing edge.

Stereo DPIV measurements were obtained by reorienting the two receivers downstream of the model, positioned symmetric about the light sheet as shown in figure 20. These locations corresponded with the locations of two of the DGV receiver components. Stereo DPIV data were acquired in a single measurement area approximately 80-x 100-mm in size near the model leading edge for a subset of the full test matrix. Since the off-body flow was predominantly two-dimensional at the tunnel centerline, the use of stereo DPIV was primarily intended to investigate the ability to obtain DPIV and DGV measurements with co-located receiver systems.

The DPIV image processing steps are outlined below. Specific details concerning the processing procedure may be found in reference 41.

1. Background image subtraction: A background, or “minimum” image was generated for each camera using a method described in reference 61. The background image was subtracted on a pixel-by-pixel basis from all captured DPIV images to reduce the influence of unwanted flare light and background noise during the analysis.
2. Pixel alignment / distortion correction: Accurate pixel registration among the various cameras comprising the DPIV and stereo DPIV receivers

was of paramount importance to minimize velocity measurement bias errors. The pixel alignment algorithm employed sequences of dot card images acquired during system calibration. The dot card images were processed using a piecewise bilinear dewarping technique originally devised to remove perspective and optical distortions for DGV images<sup>47</sup>.

3. Cross correlation analysis: Classical spatial cross correlation analysis was performed on pairs of images acquired from the two DPIV / stereo DPIV receivers using a commercially available analysis package. The relevant processing parameters used for the analysis are tabulated in Table 1.
4. Velocity field validation: Incorrect velocity vectors generated by the cross correlation analyses were identified and removed using magnitude difference algorithms contained in the shareware CleanVec validation system<sup>62</sup>. Gaussian interpolation of the validated vector fields was then performed to insert an estimated velocity vector into those interrogation regions that originally reported an incorrect velocity vector, but were surrounded by at least 50% good vectors. Regions not surrounded by 50% good vectors were unaltered.

**Table 1: DPIV / stereo DPIV Processing Parameters**

<i>Analysis Method</i>	Multiple frame cross correlation
<i>Interrogation Region Size</i>	64 Pixels square
<i>Interrogation Region Overlap</i>	50%
<i>Correlation Plane Peak Detection</i>	3-Point parabolic fit

DGV System Specifics: Once the DPIV testing was completed, two DGV receivers were installed at the identical locations as the DPIV receivers in their stereo configuration. A third DGV receiver was installed to view the light sheet via a mirror from a point above and upstream of the leading edge, figure 23. This configuration yielded out-of-plane angles greater than 41 degrees with vector-to-vector angles greater than 43 degrees. 50-mm focal length SLR lenses were used on the DGV cameras. The resulting field-of-view observable by the three DGV receiver systems was 255-x 355-mm (h-x w), beginning 25 mm in front of the model leading edge and extending downstream over the I-plate centerline.

The single-frequency, frequency-doubled Nd:YAG laser was also enclosed to protect the laser and the Laser Frequency Monitor (LFM) from the smoke and stray laser light. Two standard RS-170 compatible video cameras were used in the LFM. These cameras, in conjunction with an iodine vapor cell, were used to measure the average laser emission frequency and spatial frequency distribution throughout the laser beam cross section. This information was used to adjust the optical frequency maps obtained by the three DGV receivers, yielding images whose pixel intensity values were directly proportional to the Doppler-shifted scattered light frequency. These Doppler frequency maps were subsequently converted to 3-component velocity measurements.

The data acquisition system was configured to use four slave computers to acquire the images from the added third component and LFM. Since the original DGV data acquisition system was designed to acquire images from one to four receiver systems, the addition of the two slaves just required their activation in the software.

### TESTING PROCEDURES

The measurement systems used during the Unified Instrumentation Test were installed sequentially in the facility, and tested independently prior to operating in a unified manner with the other measurement techniques. The order of testing is shown in Table 2.

**Table 2: Testing order for the Unified Instrumentation Test**

Test #	Instruments	Operation
0	Prelim. flow visualization	Independent
1	AMA	Independent
2	PMI	Independent
3	PSP	Independent
4	DPIV	Independent
5	AMA, PMI, PSP, DPIV	Unified
6	Stereo DPIV / AMA	Unified
7	DGV	Independent
8	AMA, PMI, PSP, DGV	Unified

Each system followed an identical test matrix, designed to change the size of the flow separation bubble and reattachment location behind the wind tunnel model leading edge. This approach exercised the capabilities of each technique whether operated independently or in a unified manner. Measurements were obtained for static leading edge deflection angles ranging from 0° to

+12° in 2° increments for tunnel free stream velocities of 15, 30, and 40 m/s. Adjustment of the leading edge angle was done manually by setting the angle with a precision accelerometer, and then clamping the leading edge in place using the threaded rod and block assembly shown in figure 15. The PMI measurements acquired during tunnel runs verified that the leading edge angle did not change significantly as a result of aerodynamic loading.

Only a modest amount of synchronization was used among the instrumentation systems during unified testing. The on-body and off-body measurement techniques had significantly different data acquisition times, complicating full synchronization. AMA and pressure tap data acquisition took 25 seconds per test condition. The PMI data were acquired in approximately 5 seconds per test condition, whereas PSP data acquisition took approximately 20 seconds per test condition. DPIV and DGV data acquisition took approximately 25 minutes per test condition because of limitations imposed by the frame grabber software libraries that prevented the acquisition of more than 100 Mb of video into host memory. Thus the DPIV/DGV acquisition sequences were segmented as follows:

DPIV: 5 sets of 40 image pairs acquired at a frame rate of 2 Hz, totaling 200 image pairs per receiver or 800 images per condition (200 pairs × 4 cameras)

DGV: 4 sets of 25 image ensembles acquired at a frame rate of 10 Hz, repeated 5 times. This totaled 4000 images per condition (500 image ensembles × 8 cameras)

The DPIV/DGV data acquisition times could be dramatically reduced by upgrading the DPIV/DGV acquisition system to remove the 100 Mb software-imposed storage limitation or to enable video streaming to disk. This would reduce the DPIV/DGV acquisition times to nominally 60 seconds, more commensurate with the acquisition times of the other instrumentation systems used during this test.

A typical unified acquisition sequence was begun by arming all of the instrumentation systems. Seeding was injected into the flow and allowed to stabilize for approximately 30 seconds. The DPIV/DGV acquisition system was used to continually monitor the DPIV/DGV camera outputs. When optimal seeding levels were obtained, the DPIV/DGV data acquisition operator verbally announced the start of data acquisition, and

triggered the DPIV/DGV, AMA, and PMI acquisition computers. The PSP acquisition computer was manually triggered based on the verbal command of the DPIV/DGV acquisition system operator. PSP and PMI data were acquired at the beginning and end of the 25-minute acquisition sequence to monitor any drift that may have occurred throughout the acquisition time. No significant drift in either the tunnel velocity or leading edge angle was revealed by these techniques.

## **REPRESENTATIVE RESULTS**

### **On body: Surface Pressure Taps / AMA**

Steady state surface pressure data measured using the taps embedded in the I-plate are shown in figure 33. The data were acquired at 40 m/s tunnel free stream velocity and a model LEA of +12°. Results produced by several clogged taps have been removed for clarity. The general shape of the pressure distribution shown in figure 33 reveals information concerning the extent of the separated flow region generated by the model leading edge. The  $C_p^*$  values shown remain flat or slightly decrease along the centerline of the I-plate until approximately tap 8 to 10, at which point the pressure starts to rapidly increase and level off near tap 28. As described in reference 5, use of the  $C_p^*$  function defined in equation (2) instead of the traditional  $C_p$  function allows the mean pressure distribution from various separated flow studies to be correlated. Many of these studies (reference 5 contains six different examples) have shown that the point along the centerline of the separation bubble at which the pressure starts to increase (the lower pivot point) indicates the location of greatest separation bubble height. Furthermore, this pivot point occurs at approximately one-half of the reattachment distance. Thus, it can be inferred that reattachment for the flow condition illustrated in figure 33 will occur in the vicinity of taps 16 to 20.

The unsteady surface pressure is a further indicator of the flow reattachment location. Figure 34 presents example measurements of the RMS surface pressure fluctuations measured using the AMA. The data represent the pressure fluctuations experienced along the top-centerline of the model for a tunnel free stream velocity of 40 m/s and a +12° LEA. The RMS surface pressure fluctuations were computed by applying equation (3) to the raw microphone data. The flow reattachment location is identified by the maximum pressure unsteadiness, occurring in the vicinity of tap #20, ~254 mm downstream of the leading edge.

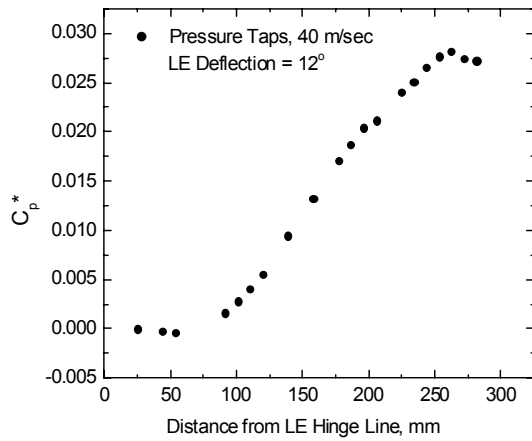


**Figure 33:** Centerline  $C_p^*$  distribution for 40 m/s tunnel free stream velocity, +12° LEA. Inoperative taps have been deleted for clarity.

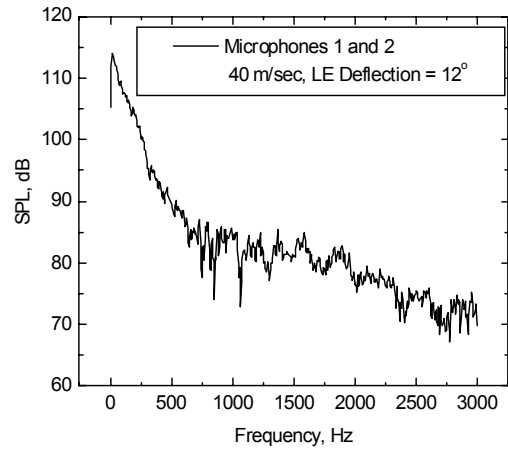


**Figure 36:** Representative cross spectrum magnitude computed for microphones #1 and #2.

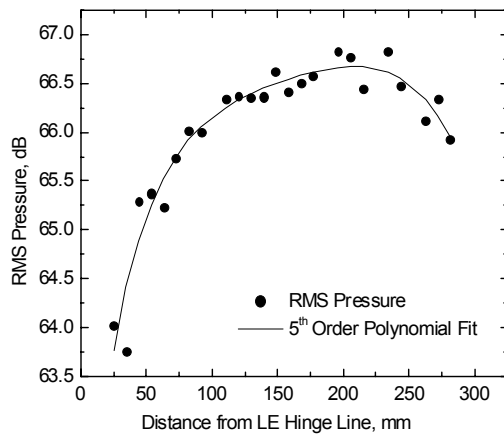


**Figure 34:** Centerline RMS pressure distribution for 40 m/s, +12° LEA.

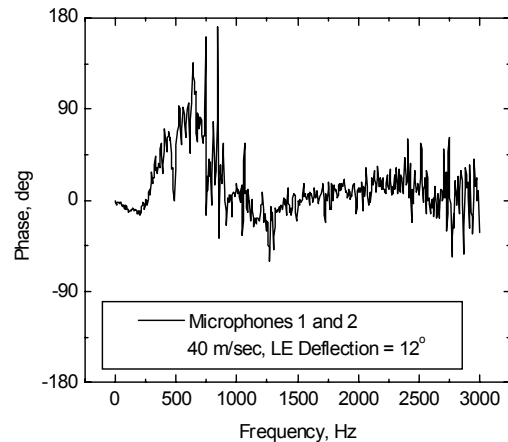


**Figure 37:** Representative cross spectrum phase computed for microphones #1 and #2.

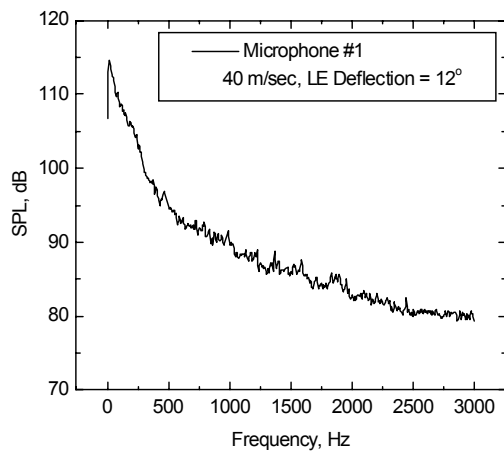


**Figure 35:** Representative auto spectrum for microphone #1.

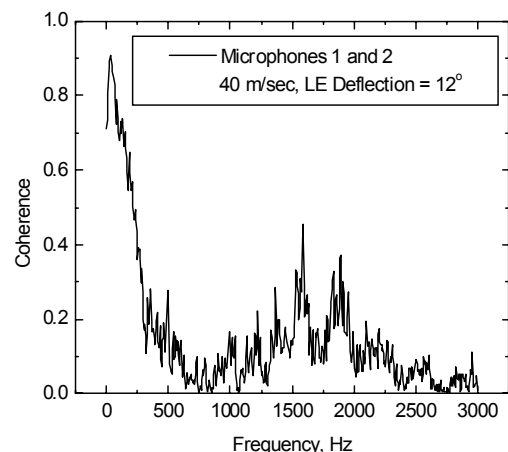


**Figure 38:** Representative coherence plot for microphones #1 and #2.

This reaffirms the conclusion drawn from the pressure tap data that flow reattachment occurred near tap #20 for this particular flow and model condition.

The microphone data were also analyzed in the frequency domain by applying equations (4) and (5) to compute the auto- and cross-spectra, and inter-channel coherence. Figure 35 shows a representative power spectrum for microphone 1 (nearest the model leading edge on the centerline) for a free stream velocity of 40 m/s and +12° LEA. As can be seen from the shape of the spectrum, the relevant spectral energy encompasses a range from DC to approximately 500 Hz. Figures 36 and 37 show representative cross spectral magnitude (figure 36) and phase (figure 37) plots for centerline microphones #1 and #2 for the same flow condition. Figure 38 shows a representative coherence function for the same microphones and flow conditions as figure 35. The coherence function clearly shows that the spectral energy in the flow (at least in the vicinity of microphones 1 and 2) decreases rapidly from DC to 500 Hz and falls off to low levels at higher frequencies.

#### **On-body: PSP**

Representative PSP data acquired at 40 m/s tunnel free stream velocity for 0, +6, and +12° model LEA are shown in figure 39. The data were acquired independent of the other measurement techniques used in the Unified Instrumentation Test. The line plots provided in figure 39 show the comparison of PSP measurements with pressure tap measurements along the model centerline. Relatively poor correlation was observed at 0° LEA, having a nominal 138 Pa total pressure change along the model surface. Excellent correlation with the pressure tap data was achieved for +12° LEA, as the total pressure change approached 690 Pa. In general, the PSP performance was suitable for characterizing the on-body characteristics and reattachment location of the separated flow generated by the model leading edge. The global nature of the PSP results provided clear visual demarcation of the flow reattachment, and these results correlated well with the reattachment location identified by the pressure tap and AMA data. The data shown in figure 39 are also typical of PSP data acquired while testing in a unified manner with the taps, AMA, and PMI, figure 40a. This confirmed that the PMI laser light did not corrupt the PSP data images or cause paint photodegradation, even when the PMI system laser was increased to its maximum output power level of 30 watts.

Unified operation with DPIV and DGV presented significantly greater challenges involving the 532-nm DPIV/DGV laser light and flow seeding. The PSP camera was equipped with a band pass filter centered about the 650 nm PSP emission peak, which provided isolation from the direct 532 nm DPIV/DGV laser illumination. However, as is shown in figure 3, the 532 nm DPIV/DGV emission lies within one of the primary PSP excitation peaks. Thus the presence of the DPIV/DGV laser light (including light scattered from seed particles) induced additional paint excitation and emission, which ultimately appeared as an artificial pressure reduction in the PSP data images. This data corruption occurred most predominantly in the vicinity of the DPIV/DGV light sheet. This effect can be seen in figure 40b, which shows a PSP image acquired in a unified manner with AMA, PMI, and DPIV at the same tunnel and model conditions as figure 40a. The presence of the 532 nm laser light and inhomogeneous seed material results in the complete loss of the pressure information in the vicinity of the I-plate, and indicates an artificial pressure reduction near the model centerline.

In an attempt to circumvent this problem, a liquid-crystal (LC) shutter was placed in front of the PSP camera. The LC shutter had an open/close time of 100  $\mu$ s, a 1000:1 contrast ratio, and 70% transmission at 650 nm. The shutter was synchronized with the DPIV/DGV laser pulse timing such that the shutter was closed for 5 ms bracketing the time when the DPIV/DGV laser was pulsed, and open for the remaining 95 ms between laser pulses. PSP data images were acquired by allowing the camera to integrate over multiple open/close cycles of the LC shutter. This approach seemed to alleviate most of the errors attributable to the laser exciting the paint. However, the spatial and temporal non-uniformity of the flow seeding continued to cause a variable attenuation in the transmitted and received PSP light collected during the open shutter periods. Figure 40c shows a PSP data image acquired in unified operation with AMA, PMI, and DPIV at the same tunnel and model conditions as figures JJ6a-b. The LC shutter was in use to remove the effects of DPIV laser excitation of the paint, and a moderate amount of seed material existed in the flow for DPIV measurements. The PSP data in figure 40c indicate that the use of the LC shutter helped to restore some of the pressure information as compared to figure 40b. However, the PSP data in figure 40c exhibits large variations in the pressure distribution compared to the no laser, no seed measurement shown in figure 40a.

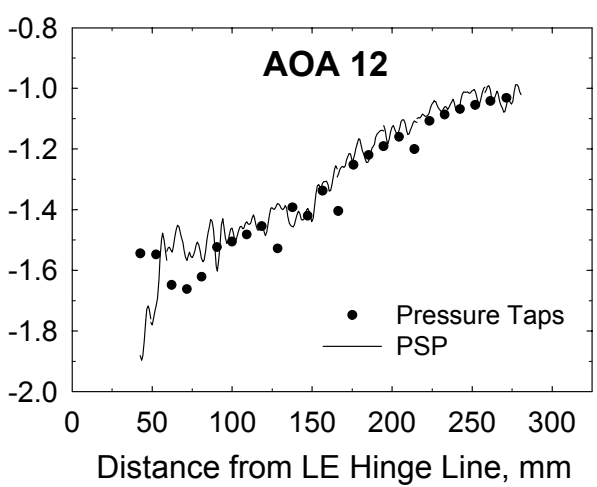
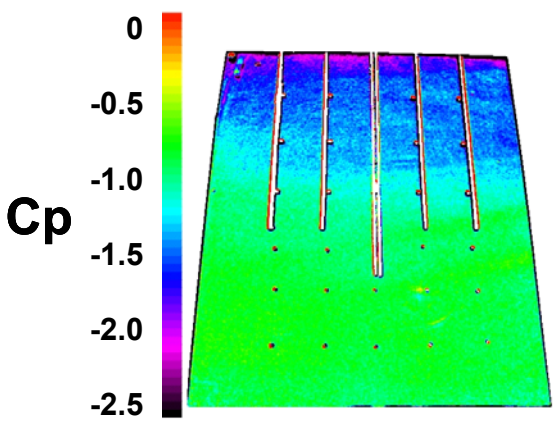
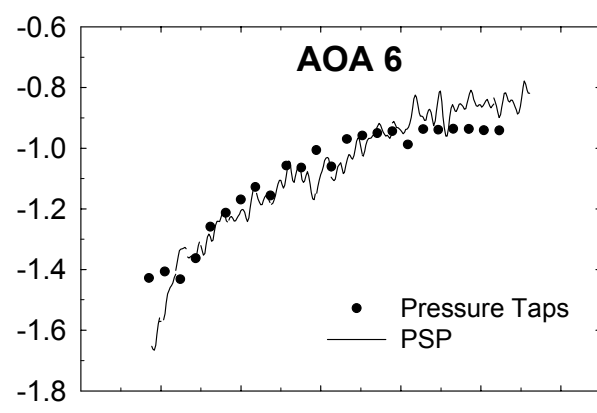
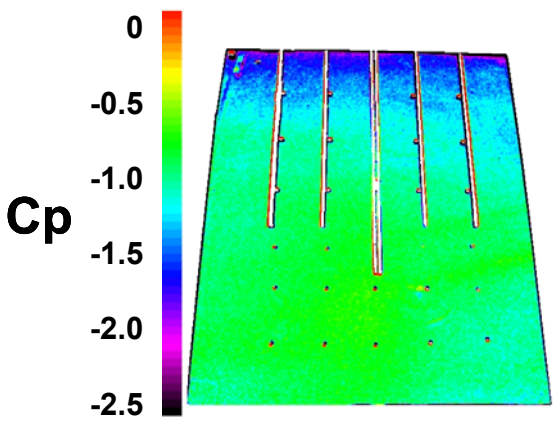
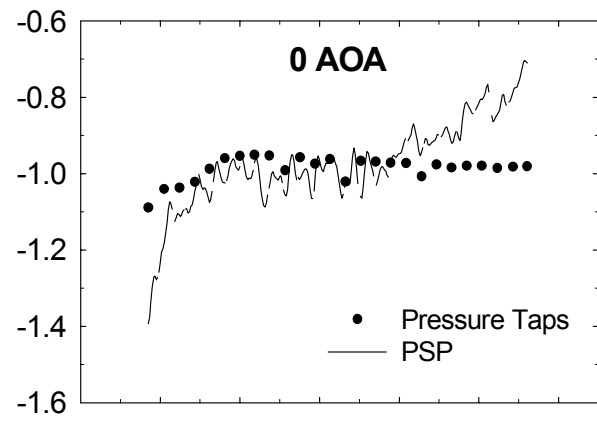
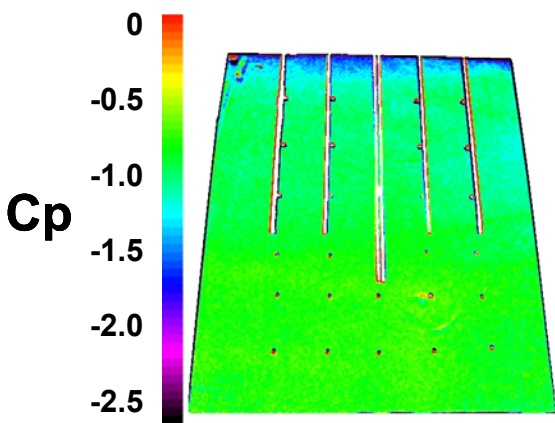
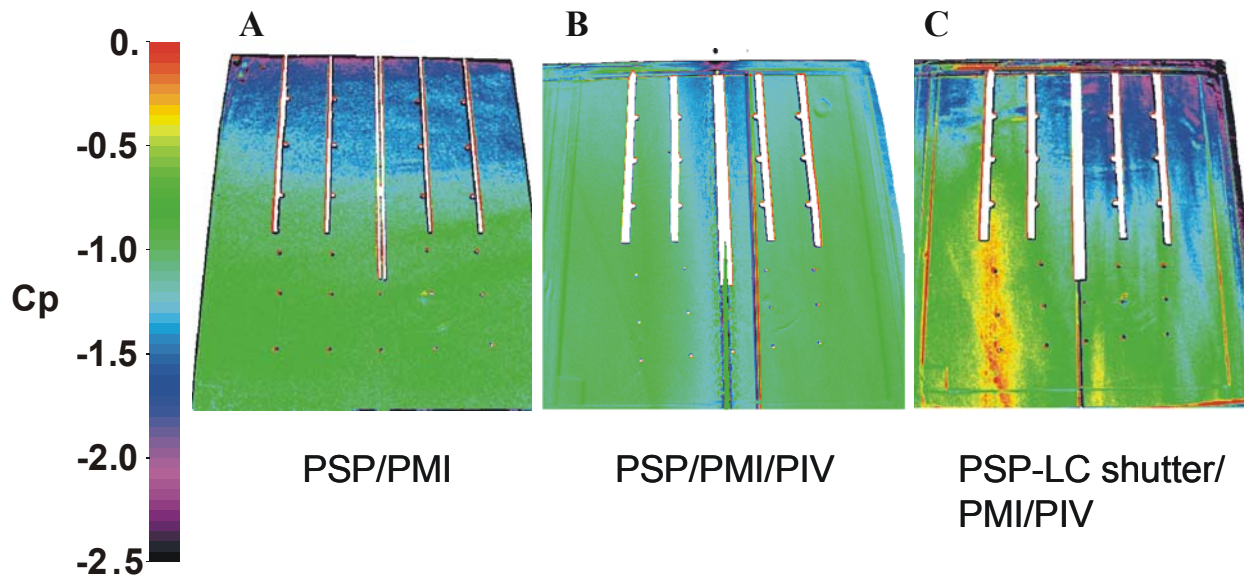


Figure 39: PSP images and chordwise line plots compared with pressure taps for leading edge deflection angles of +0, 6, and 12°.



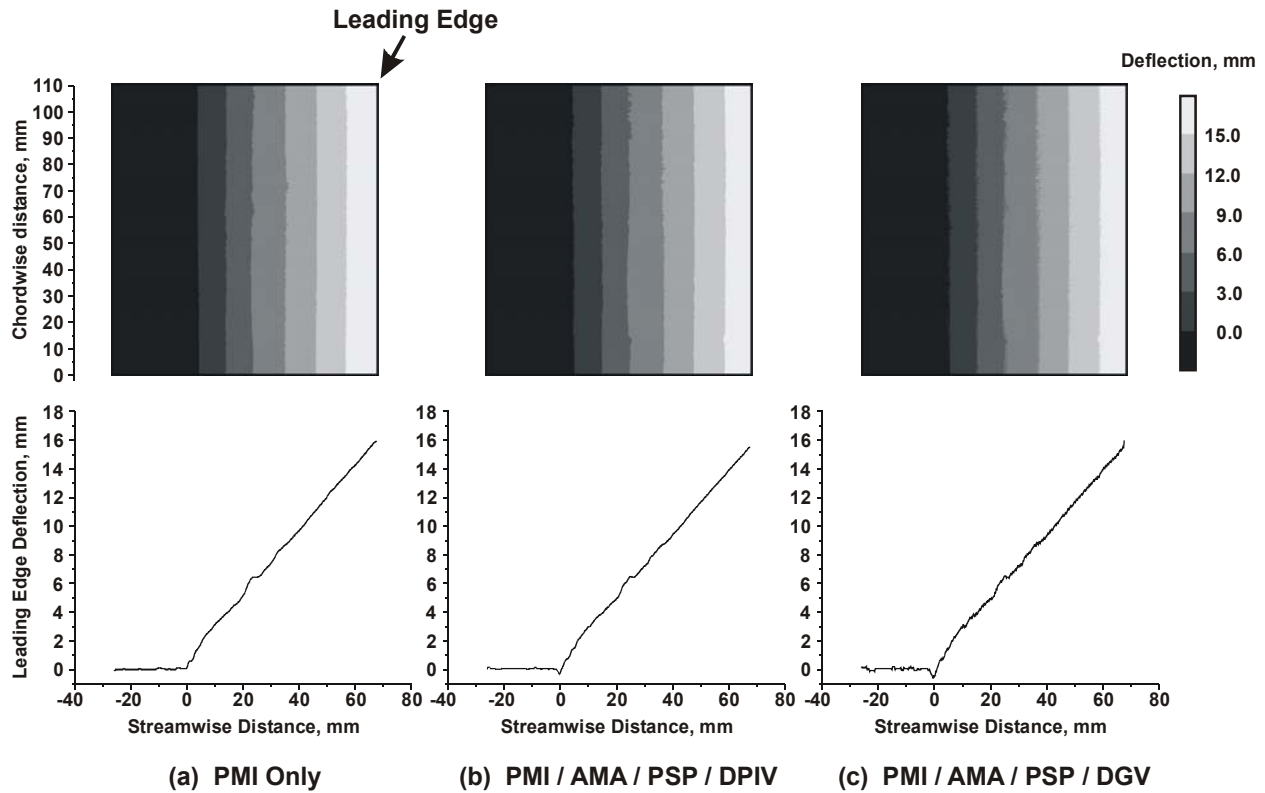
**Figures 40a - c:** (a) PSP data acquired under unified conditions with pressure taps, microphone array, and PMI, (b) effect of PIV laser and tunnel seeding on PSP data, (c) effect of acquiring PSP images between laser pulses using a liquid-crystal shutter.

Furthermore, each of 16 independent PSP data images averaged to comprise the image in figure 40c showed different spatially varying pressure distributions. Therefore the flow seeding non-uniformity completely prevented the acquisition of reliable PSP data when operating simultaneously with DPIV. This problem became worse when attempting unified operation with DGV, since DGV requires much greater seeding densities than DPIV.

**On-body: PMI**

PMI data indicative of the model leading edge deflection are shown in figures 41a-c. The data were acquired at a tunnel free stream velocity of 40 m/s and +12° LEA. Three series of plots are shown, illustrating the PMI data acquired (a) independently, (b) in unified operation with AMA, PSP, and DPIV, and (c) in unified operation with AMA, PSP, and DGV. The contour plots are the processed PMI data images, which represent the out-of-plane (vertical, in this case) deflection of the leading edge. The line plots below each contour plot show the leading edge deflection through the horizontal centerline of the PMI system field-of-view. The contour plots and line plots exhibit nearly identical behavior for the three cases shown. PMI and PSP were found to be completely compatible through all stages of testing. Additionally, the PSP provided a nearly ideal diffuse scattering surface for

PMI measurements. Thus the simultaneous application of PSP and PMI can alleviate problems caused by specular reflection of the projected grid lines when testing highly polished metallic models. The data collected during unified operation with AMA, PSP, and DGV, figure 41c, contains more high spatial frequency noise than the data shown in figures 41a-b. This noise is attributable to the relatively high seed particle density required by DGV. The noise is not apparent in figure 41b, since DPIV requires significantly lower seeding densities compared to DGV. In contrast to PSP, existence of seed material in the flow does not corrupt the PMI measurements because PMI is more dependent on spatial resolution rather than intensity resolution. Thus smoke-induced dynamic attenuation of the emitted and received PMI laser light has little effect on the measured results. Based on the data as shown in figures 41a-c, PMI was determined to be directly compatible with all of the other measurement techniques used during the Unified Instrumentation Test.



**Figures 41a - c:** PMI deformation maps and chordwise line plots of the leading edge deflection for (a) independent PMI operation, (b) unified operation with AMA, PSP, and DPIV, and (c) unified operation with AMA, PSP, and DGV.

#### **Off-body: DPIV**

Figure 42 shows a series of six velocity field streamline plots obtained using the 2-dimensional DPIV configuration. The streamline plots were derived from the processed DPIV velocity vector plots, and illustrate the off-body flow structure at 40 m/s tunnel free stream velocity and +2, 4, 6, 8, 10, and 12° LEA. The data shown in figure 42 have been cropped from the full DPIV system field-of-view to allow easier viewing of the flow structure in the vicinity of the reattachment location. The location of AMA centerline microphone #20 is shown as a reference. A comparison of the +12° LEA streamlines in Figure 42 with the RMS pressure fluctuation data shown in figure 34 shows a high degree of correlation between the reattachment locations identified by the on- and off-body instrumentation. Velocity streamline plots similar to those shown in figure 42 were also obtained while conducting unified tests with AMA, PSP, and PMI. There was no apparent contamination of the DPIV images from the PMI laser light or PSP illumination and emission.

#### **Off-body: DGV**

The acquisition of DGV measurements was first attempted independent of the other measurement techniques. During this course of testing, it became apparent that extraneous scattered DGV laser light was a critical impediment to acquiring accurate velocity measurements. Laser light scattered off the particles in the heavy smoke plume reflected off the tunnel walls and the PSP on the model surface, causing a green “glow” in the SBRT test section. Unfortunately, since DGV is basically an amplitude measurement, this secondary scatter was a direct error source since its optical frequency was different from the Doppler shifted light collected from the light sheet. The resulting measurements were the amplitude-weighted average of all optical frequencies originating from all light sources viewed by each pixel, and did not accurately represent the Doppler-shifted scattered light from particles embedded in the flow.

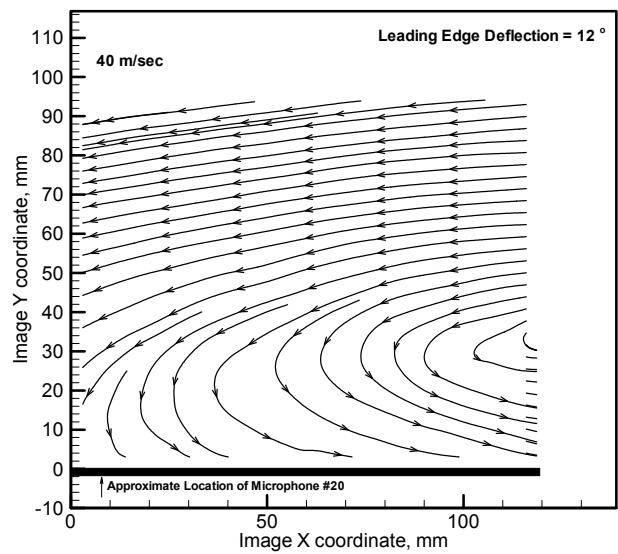
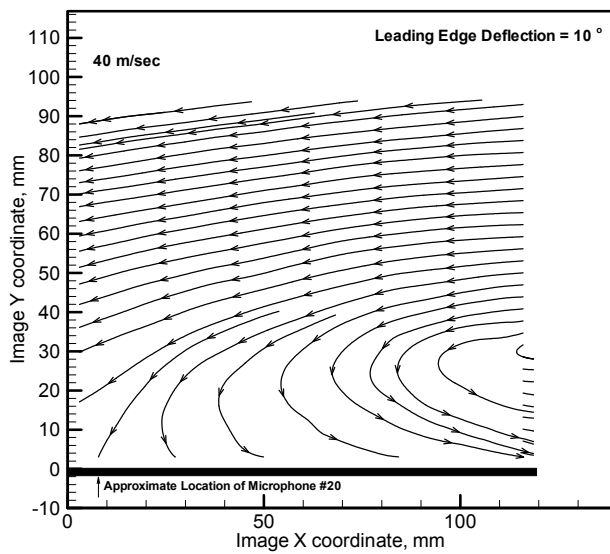
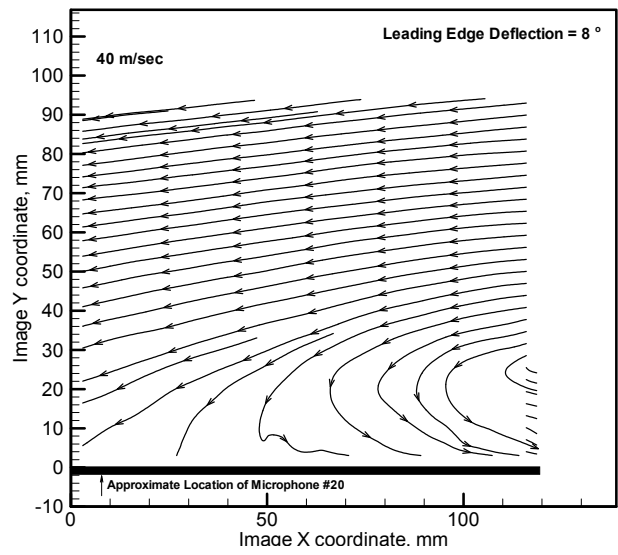
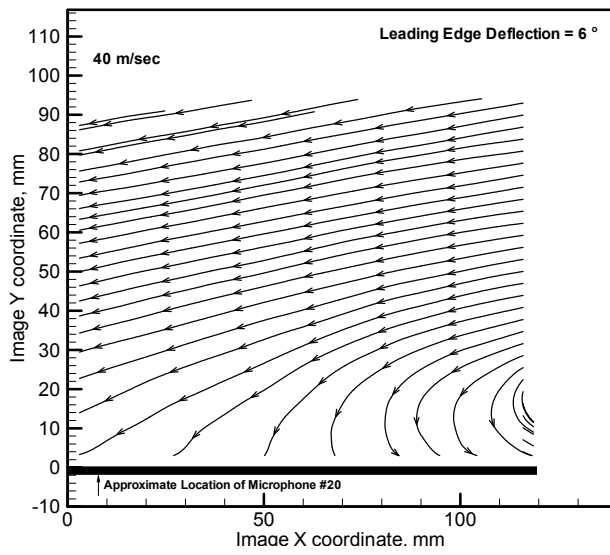
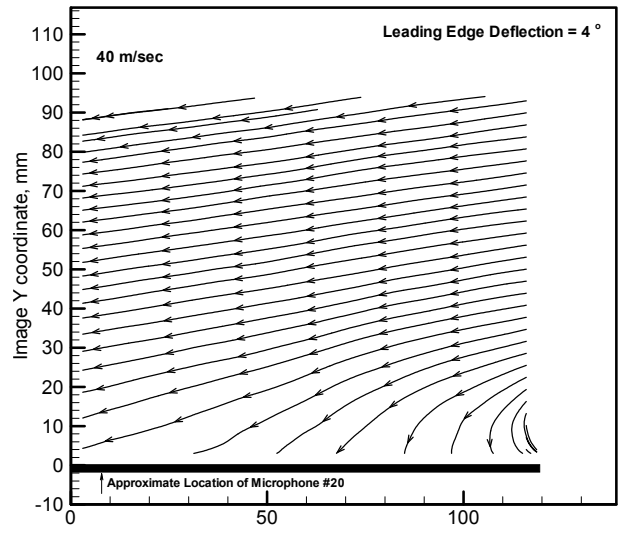
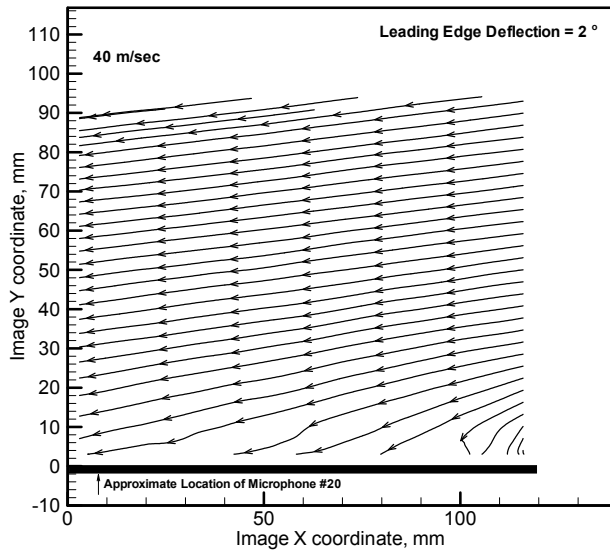


**Figure 42:** Two-component DPIV streamlines for 40 m/s free stream velocity and +2, 4, 6, 8, 10, 12° LEA.

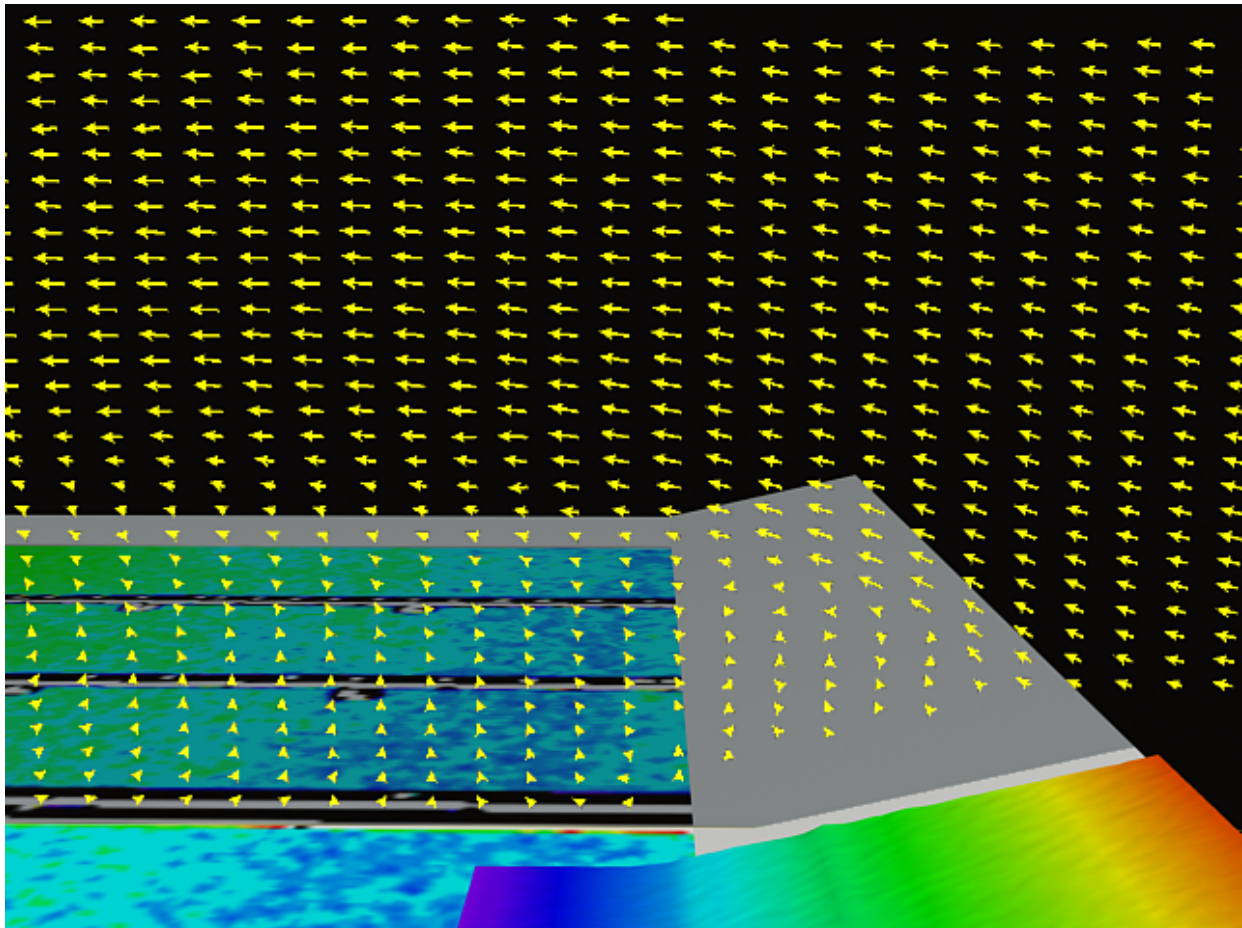


**Figure 43:** DPIV, PMI, and PSP data imported back into the VF environment for enhanced data analysis and visualization.

Several attempts were made to minimize the amount of secondary-scattered light. First, the PSP was removed from the I-plate and the I-plate was painted flat black. Most of the interior of the test section was also painted flat black. Although these steps reduced the amount of secondary scatter, it could not be completely eliminated. Thus velocity maps comparable to those obtained by DPIV could not be obtained.

The susceptibility of DGV to secondary scatter from tunnel walls and/or model surface will remain a continual issue in the development and application of the technique. Testing in small wind tunnel facilities, such as the SBRT, may pose greater challenges in overcoming problems incurred by secondary scatter than testing in larger facilities where the confining walls are farther away from the measurement area. Scattering off the model will unequivocally corrupt velocity measurements near the model surface. However, this does not preclude the acquisition of representative flow field velocity measurements well above the surface, as is shown in figure 12. The data shown in figure 12 were also acquired in the SBRT facility, albeit with a different model and optical

configuration than that used during the Unified Instrumentation Test. Thus the presence and effects of secondary scatter are fully test-dependent, and often impossible to predict. The largest difficulty with secondary scatter is that its effects are often unapparent until the data are processed. Secondary scatter often does not manifest itself in the raw DGV data images, and potential sources of secondary scatter cannot be modeled using VF technology. Therefore problems caused by this error source are often not discovered until middle- or post-test. This mandates the need for near real-time data processing, which would allow for easier identification and minimization of secondary scattering errors early in the test.

### **VF – Unifying the Results**

Efficiently analyzing and the results obtained with multiple measurement techniques can be a difficult task. For the Unified Instrumentation Test, enhanced data analysis and visualization capabilities were achieved using the VF model originally used for test planning. Figure 43 shows an example of PMI, PSP, and 2-component DPIV measurements imported back

into the VF model. Use of the 3-dimensional virtual environment for data visualization provided clear advantages for identifying aerodynamic cause and effect relationships compared to viewing the data as 2-dimensional images.

### **INSTRUMENT COMPATIBILITY SUMMARY**

The Unified Instrumentation Test revealed numerous areas where the optical measurement techniques were compatible with one another. Likewise, some unexpected incompatibilities were identified. In general, operating each instrument at different discrete optical wavelengths worked well to optically isolate the measurement techniques. Table 3 lists the operating wavelengths of the instruments used during the Unified Instrumentation Test.

**Table 3: Optical measurement techniques used in the Unified Instruments Test**

<b>Technique</b>	<b>Wavelength(s), nm</b>
PSP	400 ± 50, 650 ± 50
PMI	795
DPIV	532
DGV	532

The AMA was determined to be compatible with all of the optical measurement techniques used during the test. Naturally, optical interference between the AMA and other instrumentation systems was not a concern since AMA is not an optical instrument. However, a subtle area of potential compatibility problems involved the seed material used for DPIV/DGV. Seed material constituted of large diameter particles (e.g., propylene glycol) has a tendency to condense onto the model surface, and the deposited liquid could obstruct the microphone apertures thus affecting their response. The vaporized mineral oil seed used during the Unified Instrumentation Test showed no signs of condensation onto the model surface, and therefore did not corrupt the AMA.

PMI and PSP were found to be completely compatible through all stages of unified testing. The PSP showed no signs of photodegradation as a result of the 795 nm PMI laser light, nor could the PMI laser illumination be seen in any PSP image. Likewise, there was no evidence of the PSP ultraviolet illumination or emitted red light in the PMI images. The PSP also provided a nearly ideal diffuse scattering surface for PMI. Thus

the two techniques can be used simultaneously in future tests, which presents the possibility of using PMI measurements to correct for wind off / wind on pixel registration errors in PSP images.

PMI was also found to be compatible with both the DPIV and DGV off-body velocity measurement techniques. The PMI image quality requirements are substantially more dependent on spatial resolution than intensity resolution. Thus the presence of seed particle material within the flow at low to moderate levels does not significantly corrupt the PMI image data. Therefore PMI can readily be used to measure wind tunnel model structural deformation simultaneously with these off-body velocity techniques, a critical capability for measuring control surface actuation / aerodynamic reaction phenomena.

PSP was found to be largely incompatible with the off-body velocity techniques for two fundamental reasons: (1) non-stationary / non-uniform flow seeding caused wind-on variations in the PSP signal intensity that appeared as an artificial pressure variation, and (2) seed particle scattered light from the high powered DPIV and DGV lasers was absorbed by the PSP and emitted in the 650 ± 50 nm PSP output band. Normally the PSP photon absorption efficiency in the 532 nm region is low compared to the UV. However, the high energy of the DPIV and DGV lasers created enough light scattering to cause the PSP absorption and associated emission to be a problem. This was solved by placing a liquid crystal shutter in front of the PSP camera and closing the shutter during DPIV/DGV Nd:YAG laser pulses. The shutter minimized errors caused by the PSP absorption of the 532 nm laser light, but did not solve the artificial pressure variations caused by the non-stationary, non-uniform seeding. It is possible that PSP could be successfully applied with the off-body velocity measurement techniques if uniform seeding were achieved. In this case, the seed material would cause a uniform attenuation of the PSP illumination and emission, which would not alter the PSP performance with the exception of lower signal levels. Although completely homogeneous seeding is not typical, it can be achieved in supersonic wind tunnels that use water condensation droplets as seed material.

Although flow seeding emerged as a fundamental compatibility issue between PSP and DPIV/DGV, the use of seed material in the flow for the off-body techniques did not degrade the PSP. The flow was seeded with vaporized pharmaceutical grade mineral oil for both DPIV and DGV studies, and the PSP showed no seed particle-induced degradation whatsoever even

after multiple days of exposure. This is an important compatibility to note since it demonstrates that PSP and DPIV/DGV could be conducted during the same tunnel run if flow seeding is turned off during the acquisition of PSP measurements.

An important compatibility issue investigated during the course of the Unified Instrumentation Test concerned the performance of candidate hardware components and subsystems suitable for use in an integrated DPIV / DGV acquisition system. DPIV and DGV hardware components common for this test included the following:

- Seeding system
- Laser light sheet optical system
- Synchronization controller
- Video cameras
- Data acquisition computers and frame grabbers
- Data acquisition software

Many of these components, described in the Measurement Technique Implementation section, performed to expectations when used in the DPIV, stereo DPIV, and DGV acquisition configurations. Use of the same tunnel seeding system was initially of great concern, as it was unclear whether the small particle size would provide sufficient scattered light for capture by the DPIV cameras. These concerns were alleviated when the quality of the captured DPIV and stereo DPIV images was comparable to that obtained using more traditional DPIV seeding techniques. This verified that a common seeding system could be used in an integrated DPIV/DGV system. While the laser requirements for DPIV and DGV are different (single frequency versus double-pulse, etc.), the laser light sheet optical system proved compatible for DPIV and DGV.

The DPIV / DGV acquisition cameras proved to be somewhat troublesome for use in an integrated system. The cameras were ideal for DPIV and stereo DPIV imaging because of the high spatial resolution provided by the 1300-x 1030 pixel format sensors. However, this large pixel density and 8-bit dynamic range was less suitable for DGV since the technique is far more dependent on amplitude resolution than spatial resolution. For the Unified Instrumentation Test, the acquired DGV images were binned and stored at a resolution of 650-x 515 pixels, effectively making these high spatial resolution cameras unnecessary when used

for DGV. In contrast, the data acquisition computer and software subsystem performed exceptionally well when used for DPIV and DGV. No configuration changes were required to switch acquisition modes from DPIV to / from DGV, other than configuring two additional slave computers to acquire images from one additional DGV receiver and the laser frequency monitor.

A particular issue related to use of the integrated components in the stereo DPIV acquisition configuration concerned the placement of receivers to achieve maximum accuracy in the reconstructed out-of-plane velocity component. Note that receiver placements are also critical to DGV velocity field accuracy and that the DGV optimal placements may not always be suitable for stereo DPIV use. A consequence of these limitations in receiver placement between the two measurement systems is that a potentially small locus of acceptable positions is created which may hinder applying an integrated system in facilities with limited optical access unless the receivers are repositioned for each technique. Although the SBRT provided excellent optical access for the Unified Instrumentation Test, the locus of acceptable receiver locations was very limited because of the spatial constraints imposed by the facility. The best configuration for the two integrated stereo DPIV / DGV receivers was a symmetric, co-planar arrangement downstream of the measurement area, bisected by the light sheet. Note however that the stereo DPIV receivers do not have to reside in a co-planar configuration, nor do they have to be symmetrically placed about the light sheet. However, a co-planar, symmetric configuration reduces the mathematical complexity of reconstructing the out-of-plane velocity component.

A significant increase in off-body velocity measurement capability can be obtained for installations where an integrated DPIV/DGV hardware system can be deployed. The DGV configuration can be used to obtain large-scale flow velocity maps while the DPIV / stereo DPIV configuration can be used to obtain detailed measurements of specific regions of interest. While analysis of the data obtained using the above-mentioned integrated hardware components is on-going, the preliminary results indicate that construction of a viable integrated DPIV / DGV hardware system is feasible.

## **FUTURE DIRECTIONS FOR UNIFIED INSTRUMENTATION DEVELOPMENT**

The Unified Instrumentation Test served well to investigate the *physics* of simultaneously applying multiple optical instrumentation techniques in a wind tunnel environment. It also made it clearly apparent that significant improvements to the *mechanics* of applying multiple optical techniques simultaneously will be required for successful implementation in the future. Several notable areas requiring improvement are:

**Near real-time data processing:** An essential criterion for all of the techniques used, this will provide on-line data inspection to ensure proper instrument functionality and prevent data loss from corruption that may otherwise go unnoticed until post-test processing. Considering the current and near-future computational capabilities and the processing demands intrinsic to AMA, PMI, PSP, DPIV, and DGV, data turnaround times ranging from several seconds to several minutes seem realistic for processing complete data sets. Subsets of the data could be processed at sub-second intervals for qualitative inspection. Data processing at these rates will substantially aid in verifying instrument operation, and provide the aerodynamics researcher with rapid feedback regarding the flow and model conditions occurring in the test.

**Enhanced Data Visualization and Analysis Capabilities:** One of the most attractive features of applying multiple instruments in a unified testing scenario is the potential to use the output data streams to establish interrelationships that might otherwise go undetected when using a single measurement technique. This is most easily accomplished in a 4-dimensional (including time) virtual environment where the results produced by each measurement method can be presented simultaneously about a virtual wind tunnel model. The VF capability used during the Unified Instrumentation Test approaches this goal, but requires much tighter integration with each instrumentation system such that the data *processed* in near-real time can also be *visualized* in near real-time. The visualized results do not necessarily need to be the final processed data of highest quantitative accuracy. It is likely more important to maintain a high data presentation bandwidth, since a significant amount of insight can be gained by visualizing semi-quantitative (or qualitative) results at high data rates.

**Common Output File Format:** Importing the near-real time processed results into a virtual environment must be accomplished through the use of an output file format that is common among all of the instrumentation techniques being used. There is currently no such file format being pursued by instrument developers. Standard image formats such as JPEG, TIFF, BMP, etc. are generally insufficient for storing scientific image-based data, or one-dimensional vectored data such as that produced by the AMA. The files must not only contain the data, but information regarding spatial registration of the data (e.g. where it was acquired with respect to the model), tunnel conditions, and other model parameters. Spatial registration information is critically important so the data can be automatically positioned as it is streamed into the virtual environment. The Hierarchical Data Format (HDF)<sup>63</sup>, supported by the National Center for Supercomputing Applications (NCSA) provides these capabilities. HDF is a platform independent, self-describing file format suitable for storing single- or multi-dimensional data of any type. The format was specifically designed to store scientific data and associated metadata, and is becoming widely accepted in the scientific imaging community. Use of the HDF file format will be included in future AMA, PMI, PSP, DPIV, and DGV development efforts at NASA LaRC.

**Use of Video Transmission and Acquisition Standards:** Three different types of video cameras, video transmission protocols, and video acquisition systems were used during the Unified Instrumentation Test to accommodate PMI, PSP, and DPIV/DGV. While the differing imaging requirements of these techniques makes it impractical for them all to use the same type of camera, their data images can be transmitted and captured using standardized hardware and software. The IEEE-1394 (FireWire) and Camera Link<sup>64</sup> video transmission protocols are possible options for unified instrument development. IEEE-1394 has the advantage of a fully standardized data transmission protocol, cabling, and acquisition libraries, however it may be more suited to commercial-grade video cameras rather than scientific cameras. The Camera Link standard is still maturing, and currently offers a standardized digital transmission protocol and universal cabling. Camera Link currently does not have a standardized acquisition library, but may be more suited to handle the video streams produced by scientific-grade cameras. Both standards will continue to be researched for their applicability for unified instrumentation.

## ACKNOWLEDGEMENTS

Successful completion of the Unified Instrumentation Test required contributions from a large team of personnel, whose roles are acknowledged below:

*Scott M. Bartram*: Model design and fabrication, DPIV/SPIV/AMA support; *Angelo A. Cavone*: Electronics and video subsystems support; *Gary A. Fleming*: Project director for Unified Instrumentation Test, PMI principal investigator; *Gloria Hernandez*: Programmatic support; *William M. Humphreys, Jr.*: AMA/DPIV principal investigator; *JoAnne L. Ingram*: PSP chemistry development and application; *Luther N. Jenkins*: advisor for aerodynamics; *Jeffrey D. Jordan*: PSP principal investigator; *Mark A. Kulick*: Model design, fabrication, and installation; *Joseph W. Lee*: DGV development and support; *Stephen J. Lee*: Test implementation and data acquisition support; *Bradley D. Leighty*: PSP implementation; *James F. Meyers*: Principal investigator for Unified Instrumentation Project, DGV, and combined DGV/DPIV development; *Donald M. Oglesby*: PSP chemistry development and application; *Richard J. Schwartz*: VF modeling, preliminary flow diagnostics, data acquisition subsystem development and operation for DGV/DPIV; *Bruce W. South*: PMI implementation and data acquisition; *A. Neal Watkins*: PSP development and implementation; *Kenneth D. Wright*: Programmatic support.

## REFERENCES

1. Anon., *The NASA Aeronautics Blueprint: Toward a Bold New Era in Aviation*, National Aeronautics and Space Administration, 2002.
2. Schwartz, R. J., "Virtual Facilities: A Tool for Global Measurements", AIAA Paper No. 94-2581, *18<sup>th</sup> AIAA Aerospace Ground Testing Conference*, Colorado Springs, CO., June 1994.
3. Schwartz, R. J., "Virtual Facilities: Imaging the Flow", *Aerospace America*, Vol. 33, No. 7, July 1995.
4. Lee, I., and Sung, H. J., "Characteristics of wall pressure fluctuations in separated and reattaching flows over a backward-facing step: Part 1. Time-mean statistics and cross-spectral analyses", *Experiments in Fluids* **30**, pp. 262-272, 2001.
5. Hudy, L., "Simultaneous Wall-Pressure Array and PIV Measurements in a Separating / Reattaching Flow Region", *M.S. Master's Thesis, Michigan State University*, 2001.
6. Hudy, L., Naguib, A., Humphreys, W. M., Jr., and Bartram, S., "Wall-Pressure-Array Measurements Beneath a Separating / Reattaching Flow Region", AIAA Paper No. 2002-0579, *40<sup>th</sup> Aerospace Sciences Meeting and Exhibit*, Reno, NV, 2002.
7. Bell, J.H., Schairer, E.T., Hand, L.A. and Mehta, R.D., Surface Pressure Measurements Using Luminescent Coatings, *Annual Review of Fluid Mechanics*, 33, 2001.
8. McLachlan, B.G. and Bell, J.H., Pressure-Sensitive Paint in Aerodynamic Testing, *Experimental Thermal and Fluid Science*, 10, 1995.
9. Crites, R.C. (1993), Measurement Techniques—Pressure Sensitive Paint Technique, Lecture Series 1993-05, Von Karman Institute for Fluid Dynamics.
10. Engler, R.H., Klein, C., 1997, DLR PSP System Intensity and Lifetime Measurements. Presented at the 17<sup>th</sup> International Congress on Instrumentation in Aerospace Simulation Facilities (ICIASF), Pacific Grove, CA.
11. Liu, T., Campbell, B.T., Burns, S.P., and Sullivan, J.P., Temperature- and Pressure-Sensitive Paints in Aerodynamics, *Applied Mechanics Reviews*, 50, 1997.
12. Bykov, A., Fonov, S., Mosharov, V., Orlov, A., Pesetsky, V., and Radchenko, V. (1997), Study Result for the Application of Two-Component PSP Technology to Aerodynamic Experiment, AGARD Conference Proceedings CP-601, *Advanced Aerodynamic Measurement Technology*, 29-1 to 29-8.
13. Donovan, J. F., Morris, M. J., Pal, A., Benne, M. E. and Crites, R. C. (1993), Data Analysis Techniques for Pressure- and Temperature-Sensitive Paint, AIAA Paper 93-0176.
14. Asai, K., Kanda, H., and Kunimasu, T., (1996), Detection of Boundary-Layer Transition in a Cryogenic Wind Tunnel by Using Luminescent Paint, AIAA Paper 96-2185.
15. Holmes, J., Analysis of Radiometric, Lifetime and Fluorescent Lifetime Imaging for Pressure Sensitive Paint. *Aeronautical J.* April (1998).

16. Kavandi, J., Callis, J., Gouterman, M., Khalil, G., Wright, D. Luminescent Barometry in Wind Tunnels, *Review of Scientific Instrumentation*, 61, 1990.
17. Le Sant, Y., Merienne, M-C. 1995. An Image Resection Method Applied to Mapping Techniques. Presented at the 16<sup>th</sup> International Congress on Instrumentation in Aerospace Simulation Facilities (ICIASF), Dayton, OH.
18. Lakowicz, J.R., *Principles of Fluorescence Spectroscopy*, Plenum Press, New York, 1983.
19. Bell, J.H and McLachlan, B.G. Image Registration for Pressure Sensitive Paint Applications. *Experimental Fluids*, 20, 1996.
20. Bradley, L. C. (1995), A Temperature-Sensitive Phosphor Used to Measure Surface Temperature in Aerodynamics, *Rev. Sci. Instrum.* 24(3), 219-220.
21. Bykov, A., Fonov, S., Mosharov, V., Orlov, A., Pesetsky, V., and Radchenko, V. (1997), Study Result for the Application of Two-Component PSP Technology to Aerodynamic Experiment, AGARD Conference Proceedings CP-601, Advanced Aerodynamic Measurement Technology, 29-1 to 29-8.
22. Donovan, J. F., Morris, M. J., Pal, A., Benne, M. E. and Crites, R. C. (1993), Data Analysis Techniques for Pressure- and Temperature-Sensitive Paint, AIAA Paper 93-0176.
23. Harris, J., and Gouterman, M. (1995), Referenced Pressure Sensitive Paint, Flow Visualization VII, Proceeding of the Seventh International Symposium on Flow Visualization, edited by J. Crowder, Seattle, Washington, p.802.
24. Jordan, J. D., Watkins, A. N., Weaver, W. L., Dale, G. A., and Navarra, K. R., (1999), Sol-Gel-Based Pressure-Sensitive Paint Development, AIAA Paper 99-0566, Reno, NV.
25. Lyonnet, M. The Two-Component PSP Investigation On a Civil Aircraft Model in S2MA Wind Tunnel; Pressure-Sensitive Paint ONERA, TP no. 1997-101, Pressure Sensitive Paint Workshop, 5th, Arnold AFB, TN May 14-16, 1997.
26. Oglesby, D. M., Leighty, B. D. and Upchurch, B. T. (1995), Pressure Sensitive Paint With an Internal Reference Luminophore, Proceedings of the 41st International Instrumentation Symposium, Instrument Society of America, Denver, CO, 381-395.
27. Oglesby, D. M., Upchurch, B. T., Leighty, B. D. and Simmons, K. A. (1996), Pressure Sensitive Paint With Internal Temperature Sensing Luminophore, Proceedings of the 42nd International Instrumentation Symposium, Instrument Society of America, San Diego, CA.
28. Oglesby, D. M., West, J. P., Upchurch, B. T., Leighty, B. D., Pressure Sensitive Paint with Internal Correction for Light and Temperature, International Instrumentation Symposium, 44th, Reno, NV May 3-7, 1998, Proceedings; Research Triangle Park, NC, Instrument Society of America, 1998, p. 591-603.
29. Schanze, K. S., Carroll, B. F., Korotkevitch, S., and Morris, M. (1997), Temperature Dependence of Pressure Sensitive Paints, AIAA J., Vol. 35, No. 2, February, 306-310.
30. Woodmansee, M. A.; Dutton, J. C. Treating temperature-sensitivity effects of pressure-sensitive paint measurements, *Experiments in Fluids* (0723-4864), 24, 1998, p. 163-174.
31. Fonov, S.; Crafton, J.; Goss, L.; Jones, G.; Fonov, V., "Near-Real-Time Pressure-Field Visualization," ICIAFS 2001 Record, 19th International Congress on Instrumentation in Aerospace Simulation Facilities, pp. 1-4.
32. Jordan, J.D. and Oglesby, D.M. US Patent Application No. 09/558,722. "Temperature Independent Pressure Sensitive Paints," filed April 26, 2000.
33. Patorski, K., *Handbook of the Moiré Fringe Technique*, Elsevier Science Publishers, 1993.
34. Fleming, G. A., and Gorton, S. A., "Measurement of rotorcraft blade deformation using Projection Moiré Interferometry", *Journal of Shock and Vibration*, Vol. 7, No. 3, 2000.

35. Fleming, G. A., Soto, H. L., and South, B. W., "Projection Moiré Interferometry for Rotorcraft Applications: Measurements of Active Twist Rotor Blades", Proceedings of the American Helicopter Society 58<sup>th</sup> Annual Forum, Montreal, Canada, June 11-13, 2002.
36. Fleming, G. A., Bartram, S. M., Waszak, M. R., and Jenkins, L. N., "Projection Moiré Interferometry Measurements of Micro Air Vehicle Wings", Proceedings of SPIE, Vol. 4448, pp. 90 – 101, 2001.
37. Fleming, G. A., and Burner, A. W., "Deformation measurements of smart aerodynamic surfaces", Proceedings of SPIE, Vol. 3783, pp. 228 – 238, 1999.
38. Fleming, G. A., Soto, H. L., South, B. W., and Bartram, S. M., "Advances in Projection Moiré Interferometry Development for Large Wind Tunnel Applications", SAE Paper No. 1999-01-5598, SAE World Aviation Congress, San Francisco, CA, October 19-21, 1999.
39. Pirodda, L., "Shadow and projection moiré techniques for absolute or relative mapping of surface shapes", *Optical Engineering* **21**(4), pp. 640 - 649, July/August 1982.
40. Grant, I., Owens, E., and Yan, Y., "Particle Image Velocimetry Measurements of the Separated Flow Behind a Rearward-Facing Step", *Experiments in Fluids*, Volume 12, pp. 238-244, 1992.
41. Humphreys, W. M., Jr., and Bartram, S., "Measurement of Separated Flow Structures Using a Multiple-Camera DPIV System", *Proceedings of the 19<sup>th</sup> International Congress on Instrumentation in Aerospace Simulation Facilities (ICIASF)*, Cleveland, Ohio, 2001.
42. Raffel, M., Willert, C., and Kompenhans, J., *Particle Image Velocimetry - A Practical Guide*, Springer-Verlag, New York, 1998.
43. Stanislas, M., Kompenhans, J., and Westerweel, J. (Eds.), *Particle Image Velocimetry, Progress Towards Industrial Application*, Kluwer Academic Publishers, Boston, 2000.
44. Samimy, M., and Wernet, M. P., "Review of Planar Multiple-Component Velocimetry in High-Speed Flows", *AIAA Journal*, Volume 38, Number 4, pp. 553-574, 2000.
45. Westerweel, J., "Fundamentals of Digital Particle Image Velocimetry", *Measurement Science and Technology*, Volume 8, pp. 1379-1392, 1997.
46. Komine, H.: *System for Measuring Velocity Field of Fluid Flow Utilizing a Laser -Doppler Spectral Image Converter*, US Patent 4 919 536, 1990.
47. Meyers, J. F.: *Doppler Global Velocimetry - The Next Generation?* AIAA 17<sup>th</sup> Aerospace Ground Testing Conference, paper AIAA-92-3897, Nashville, TN, July 6-8, 1992
48. Meyers, J. F.: *Development of Doppler Global Velocimetry as a Flow Diagnostics Tool*, Measurement in Fluids and Combustion Systems, Special Issue, Measurement Science and Technology, vol. 6, no. 6, pp. 769-783, June 1995.
49. Roehle, I: *Three-dimensional Doppler Global Velocimetry in the Flow of a Fuel Spray Nozzle and in the Wake Region of a Car*. Flow Measurements Instrumentation vol. 7, pp. 287-294, 1996.
50. Meyers, J. F.: *Evolution of Doppler Global Velocimetry Data Processing*. Eighth International Symposium on Applications of Laser Techniques to Fluid Mechanics, paper 11.1, Lisbon, Portugal, July 8-11, 1996.
51. Reinath, M. S.: *Doppler Global Velocimetry Development for the Large Wind Tunnels at Ames Research Center*. NASA TM-112210, 1997.
52. Komine, H.; Brosnan, S. J.; Long, W. H.; and Stappaerts, E. A.: *Doppler Global Velocimetry Development of a Flight Research Instrumentation System for Application to Non-intrusive Measurements of the Flow Field*, NASA Report CR-191490, 1994.
53. Elliott, G. S.; Samimy, M.; and Arnette, S. A.: *A Molecular Filter Based Velocimetry Technique for High Speed Flows*. Experimental Fluids, vol. 18, pp. 107-118, 1994.
54. McKenzie, R. L.: *Planar Doppler Velocimetry for Large-Scale Wind Tunnel Applications*. AGARD Fluid Dynamics Panel 81<sup>st</sup> Meeting and Symposium on Advanced Aerodynamic Measurement Technology, paper 9, Seattle, WA, September 22-25, 1997.

55. Smith, M. W.: *Application of a Planar Doppler Velocimetry System to a High Reynolds Number Compressible Jet*. AIAA 36<sup>th</sup> Aerospace Sciences Meeting & Exhibit, paper AIAA 98-0428, Reno, NV, January 12-15, 1998.
56. Beutner, T. J.; Elliott, G.; Mosedale, A.; and Carter, C: *Doppler Global Velocimetry Applications in Large Scale Facilities*. AIAA 20<sup>th</sup> Advanced Measurement and Ground Testing Conference, AIAA Paper 98-2608, Albuquerque, NM, 1998.
57. Elliott, G. S. and Beutner, T. J.: *Molecular Filter Based Planar Doppler Velocimetry*. Prog. Aerospace Science, vol. 35, pp. 799-845, 1999.
58. Samimy, M. and Wernet, W. P.: *Review of Planar Multiple-Component Velocimetry in High-Speed Flows*. AIAA Journal, vol. 38, pp. 553-574, 2000.
59. Meyers, J. F.; Lee, J. W.; and Schwartz, R. J.: *Characterization of Measurement Error Sources in Doppler Global Velocimetry*. Measurement Science and Technology, vol. 12, no. 4, pp. 357-368, April 2001.
60. Roshko, A., and Lau, J. C., "Some Observations on Transition and Reattachment of a Free Shear Layer in Incompressible Flow", *Proceedings of the 1965 Heat Transfer and Fluid Mechanics Institute*, Stanford University Press, 1965.
61. Kuhn, W., Kompenhans, J., Monnier, J. C., "Full Scale PIV Test in an Industrial Facility", *Particle Image Velocimetry, Progress Towards Industrial Application*, Kluwer Academic Publishers, Boston, pp. 91-150, 2000.
62. Soloff, S., and Meinhart, C., *CleanVec: PIV Vector Validation Software, Version 1.13 Build 41*, Released 1999 by Laboratory for Turbulence and Complex Flow, University of Illinois – Urbana.
63. Anon., *The HDF Home Page*, <http://hdf.ncsa.uiuc.edu/>, National Center for Supercomputing Applications, University of Illinois at Urbana – Champaign, 2002.
64. Anon., "Camera Link – Specifications of the Camera Link Interface Standard for Digital Cameras and Frame Grabbers", PULNiX America, Inc., 2000.